REPORT DOCUMENTATION PAGE

1

Form Approved OMB NO. 0704-0188

1. REPORT DATE (DD-MM-YYYY)
29-08-2014

2. REPORT TYPE
Ph.D. Dissertation

3. DATES COVERED (From - To)
-

4. TITLE AND SUBTITLE
Unconventional Density Wave and Superfluidity in Cold Atom Systems

5a. CONTRACT NUMBER
W911NF-13-1-0119

5b. GRANT NUMBER

5c. PROGRAM ELEMENT NUMBER
206022

5d. PROJECT NUMBER

5e. TASK NUMBER

5f. WORK UNIT NUMBER

6. AUTHORS
Chen-Yen Lai

7. PERFORMING ORGANIZATION NAMES AND ADDRESSES
University of California - Riverside
200 University Office Building

Riverside, CA 92521 -0001

8. PERFORMING ORGANIZATION REPORT NUMBER

9. SPONSORING/MONITORING AGENCY NAME(S) AND ADDRESS (ES)
U.S. Army Research Office
P.O. Box 12211
Research Triangle Park, NC 27709-2211

10. SPONSOR/MONITOR'S ACRONYM(S)
ARO

11. SPONSOR/MONITOR'S REPORT NUMBER(S)
62897-PH-REP.4

12. DISTRIBUTION AVAILABILITY STATEMENT
Approved for public release; distribution is unlimited.

13. SUPPLEMENTARY NOTES
The views, opinions and/or findings contained in this report are those of the author(s) and should not contrued as an official Department of the Army position, policy or decision, unless so designated by other documentation.

14. ABSTRACT

Ultra-cold atom system provides novel technology to simulate traditional solid state physics, including boson and fermion particles. Due to the flexibility of tuning parameters, people can further understand basic physics behind strongly correlated effects, especially mechanism of unconventional density wave and superfluidity. Using weak coupling renormalization group method, we propose and study several models which can be realized in experiments. Ranging from most well-known extended Hubbard model, to spin-polarized Fermi Hubbard model and multi-flavor Fermi-Fermi mixture, we establish solid theories to explain the origin of new

15. SUBJECT TERMS
cold atoms, optical lattices, Hubbard model, fermion mixture, unconventional density wave, superfluidity, superconductivity, renormalization group

16. SECURITY CLASSIFICATION OF:

a. REPORT	b. ABSTRACT	c. THIS PAGE	17. LIMITATION OF ABSTRACT	15. NUMBER OF PAGES
UU	UU	UU	UU	

19a. NAME OF RESPONSIBLE PERSON
Shan-Wen Tsai

19b. TELEPHONE NUMBER
951-827-1057

Standard Form 298 (Rev 8/98)
Prescribed by ANSI Std. Z39.18

Report Title

Unconventional Density Wave and Superfluidity in Cold Atom Systems

ABSTRACT

Ultra-cold atom system provides novel technology to simulate traditional solid state physics, including boson and fermion particles. Due to the flexibility of tuning parameters, people can further understand basic physics behind strongly correlated effects, especially mechanism of unconventional density wave and superfluidity. Using weak coupling renormalization group method, we propose and study several models which can be realized in experiments. Ranging from most well-known extended Hubbard model, to spin-polarized Fermi Hubbard model and multi-flavor Fermi-Fermi mixture, we establish solid theories to explain the origin of new states of matter, and the experimental techniques to exploit them. The effects of lattice structure and particle density in fermionic system play important roles for determining phase diagram in low energy scale. Due to the presence of lattice, these systems have insulator phase at half-filling. The density imbalance, however, prevents formation of conventional density wave state, and the screening interaction dramatically affects other species's behavior. The interplay between screening interaction and square lattice is key ingredient of unconventional density wave and superfluidity. Our study shows that the unconventional density wave and superfluidity can be realized and detected in ultra-cold atom experiments.

UNIVERSITY OF CALIFORNIA
RIVERSIDE

Unconventional Density Wave and Superfluidity in Cold Atom Systems

A Dissertation submitted in partial satisfaction
of the requirements for the degree of

Doctor of Philosophy

in

Physics

by

Chen-Yen Lai

June 2014

Dissertation Committee:

Professor Shan-Wen Tsai, Chairperson
Professor Kirill Shtengel
Professor Vivek Aji

The Dissertation of Chen-Yen Lai is approved:

Committee Chairperson

University of California, Riverside

Acknowledgments

First I would like to deeply thank my adviser, Professor Shan-Wen Tsai. This thesis would not have been possible without her guidance and patience. She has always been available when I needed help, ranging from technical details to conceptual understanding of physics and overall strategies of research. She also taught me the main principles of independent research, how to write papers that could hopefully be interesting to others, and how to maneuver through the political maze of journal peer-review publication.

I also thank my dissertation committee members, Professor Vivek Aji and Professor Kirill Shtengel, for their help, kindness, insightful comments and invaluable advices. My thanks also go to the collaboration and help from many of my colleagues at University of California, Riverside. In particular Dr. Chuntai Shi and Dr. Wen-Min Huang have been very kind to answer my questions and to discuss on my newest ideas. Special thanks goes to Professor David K Campbell of Boston University. I appreciate the work we did together during my fourth year and fruitful discussion in several March Meeting occasions. I must also thank all the people I have met at conferences and workshops during the past five years. Finally I like to thank my wife and my family for their endless support and affection.

I acknowledge support of computational resources from Professor Pochung Chen of National Tsing Hua University and National Center of Theoretical Science, Taiwan. Part of the research presented in this dissertation are published in Physical Review B of American Physics Society, and financially supported by NSF under Grant DMR-0847801, from the UC-Lab FRP under Award number 09-LR-05-118602, and from the Army Research Office, Department of Defense under Award Number W911NF-13-1-0119.

Kám-siā guá–ê pē-bú, khan-tshiú, hàu-senn^{n}, ì-kip sóo-iú guá-ài–ê lâng.

ABSTRACT OF THE DISSERTATION

Unconventional Density Wave and Superfluidity in Cold Atom Systems

by

Chen-Yen Lai

Doctor of Philosophy, Graduate Program in Physics
University of California, Riverside, June 2014
Professor Shan-Wen Tsai, Chairperson

Ultra-cold atom system provides novel technology to simulate traditional solid state physics, including boson and fermion particles. Due to the flexibility of tuning parameters, people can further understand basic physics behind strongly correlated effects, especially mechanism of unconventional density wave and superfluidity. Using weak coupling renormalization group method, we propose and study several models which can be realized in experiments. Ranging from most well-known extended Hubbard model, to spin-polarized Fermi Hubbard model and multi-flavor Fermi-Fermi mixture, we establish solid theories to explain the origin of new states of matter, and the experimental techniques to exploit them. The effects of lattice structure and particle density in fermionic system play important roles for determining phase diagram in low energy scale. Due to the presence of lattice, these systems have insulator phase at half-filled. The density imbalance, however, prevents formation of conventional density wave state, and the screening interaction dramatically affects other species's behavior. The interplay between screening interaction and square lattice is key ingredient of unconventional density wave and superfluidity. Our study shows that the unconventional density wave and superfluidity can be realized and detected in ultra-cold atom experiments.

Contents

List of Figures

Chapter 1

Introduction

Theoretical Condensed Matter Physics (CMP) strives to understand the properties and behaviors of matter. One of most intriguing phenomena of interacting quantum many-body systems in CMP is the emergence of new states of matter and competition between different types of order. From a methodological view, a physical system would be very desirable for developing, understanding and verifying a theory if it can be described with as few tunable parameters as possible. The spectacular progress of experiments has provided a new arena for studying correlated quantum many-body phenomena, where the microscopic Hamiltonian can be realized, and in addition, the parameters are possibly controllable by tuning external fields [1]. Various lattice structure, including cubic, honeycomb, and kagome, can also be realized by different sets of counter propagating lasers [2]. Comparing to conventional solid state materials, these techniques can provide a clean and controllable environment which is closed to theoretical model. One might hope that this reliable technique can shed the light on discovering insightful physics of the emergence of new states of matter.

The problem of understanding physical mechanism in strongly correlated fermionic system, like metal-insulator transition, origins of anti-ferromagnetism and superconductivity, remains an important challenge. Despite the large effort in the literature, many issues still remain controversial, mainly because of the absence of unbiased and reliable theoretical methods for handling the strong correlation problem. In the weak coupling case, at least in principle it is tractable by perturbative techniques. The main idea of renormalization group (RG) is integrating out the high energy modes, and obtaining a low energy scale physics in CMP. The famous review article [3] provides a basic idea and procedure on this treatment. It is clear that further investigation is interesting and necessary for complicated solid state materials and novel fermionic system in ultra-cold gas experiment.

In order to understand the origin of unconventional density wave and superfluid, we propose and study several models which can be realized in ultra-cold atom experiment. Considering the lattice structure and particle density in correlated fermions system, such as extended Hubbard model, spin-polarized Hubbard model, and quantum degenerate Fermi-Fermi mixture, we conclude that effective long range interaction and density imbalanced are the key to formation of unconventional density wave and superfluid in low energy scale. The experimental setup and detection of different phases are discussed in each cases.

The present dissertation is divided as follows: Chapter 2 reviews several important concepts and techniques used in the thesis. Chapters 3 to 6 then present my main work. Chapter 7 gives summary and Appendix A provides more details discussed in Chapter 2.

More specifically, in chapter 2, we briefly summarize the procedure of RG method on weakly interacting fermion system. By integrating out the thin energy shell systematically on one-loop RG equation for four point vertex, we arrive a series of effective Hamiltonians at different RG scale as we proceed this systematic process. According to the proper symmetry of the problem and background knowledge, we can define different instability channels, for instance, density wave or superconductivity, then we can analyze these channels and determine any instabilities of the system.

In chapter 3, we study the phase diagram of the extended Hubbard model on a two-dimensional square lattice, including on-site (U) and nearest-neighbor (V) interactions, at weak couplings [4]. Despite there were several studies on Hubbard model by using functional renormalization group (FRG) [5, 6, 7], the phase diagram of the extended Hubbard model was still missing. Upon different filling fractions, on-site U and nearest-neighbor V interactions, we found several instabilities, including the well known charge(spin)-density wave phase at half filling, d_{xy}-wave superconducting, and $d_{x^2-y^2}$ pairing state under slightly doping. One of most intriguing results is triplet time-reversal breaking ($p_x + ip_y$)-wave pairing instability merges. This results suggest that zero-energy Majorana modes can be realized on a square lattice. Considering a system of cold fermionic atoms on a two-dimensional square optical lattice, both an on-site repulsion and a nearest-neighbor attraction would be required, in addition to rotation of the system to create vortices. We discussed possible ways of experimentally engineering the required interaction terms in a cold atom system.

In chapter 4, we apply this RG idea on Hubbard model [8] with spin imbalanced [9]. Experiments with ultra-cold atoms have realized mixtures of two different species of fermionic atoms with different densities, including mixtures of cold lithium atoms (^{6}Li) with different populations for two different hyperfine states [10, 11]. With the presence of square optical lattice, we can model such a system as a Hubbard model where the spin-up and spin-down particle has different densities. Comparing to the imbalanced Fermi gas (without lattice), the lattice effect can provide much richer physics and accessible critical temperature. We are the first group obtain the phase diagram for this system, focusing on the case where the majority species stays close to half-filling and the density of the minority species is varied. We found several new phases, including a stripe-CDW phase and triplet pairing phases for both species. The interplay between lattice effect and the density-imbalanced provides important features for quantum correlated system. Also, the critical temperature of each phase is experimentally accessibility and much higher than the one without lattice.

In chapter 5, we proposed and studied a quantum degenerate Fermi-Fermi mixture model on square lattice [12]. According to recent experiments, a system with different types of quantum degenerate fermionic atom can be engineered, for instance, ^{6}Li and ^{40}K [13]. In this two-species Hubbard model, both inter-species and intra-species interactions are taken into account at equal footing. Unlike the usual single-species (orbital) model, the competition between inter-species and intra-species interaction provides more intriguing strongly correlated effect. Our study shows the various dominant instabilities under different interaction ratios and the number density imbalance between different atoms. One of exciting result is the unconventional d_{xy}-wave charge density wave, which lives in a very wide parameter regime of the phase diagram and has an accessible critical temperature.

Most importantly, our theory provides a general screening mechanism of forming this kind of exotic phase on a square lattice. This study sheds the light on searching unconventional density wave for a minimum on-site Hubbard model.

In chapter 6, we use FRG method to study a dipolar fermion system on a square lattice of bilayer. The recent experiment is able to prepare electric [94] or magnetic dipoles [93] in a magneto atomic trap. The former can also be loaded onto optical lattice [117]. The intriguing long-range interaction already draw a lot of attention on theoretical studies [121, 122, 123, 124, 125, 126, 127]. On a two dimensional square lattice, this kind of system was studied before [83, 100] as well. In the two dimensional plane, the phase diagram can be interpreted by two critical angles [83]. Also, this long-range anisotropic interaction drives the system into some unconventional density and pairing ground states when the dipoles are oriented in particular polar angles. Due to the anisotropic nature of dipole-dipole long-range interaction, the presence of second layer brings up the interplay between intra- and inter-layer interactions, which makes this system more interesting than monolayer system. Also, the unconventional charge density wave is found in wilder range in phase diagram than one in monolayer square lattice.

Conclusions and outlook are given in chapter 7. The back-matter contains appendix and the bibliography.

Chapter 2

Functional Renormalization Group for Interacting Fermion

2.1 Renormalization Group Method

The functional renormalization group approach to interacting fermions[3, 5, 6] has been applied to the study of the stability and instabilities of Fermi liquids. Starting with a microscopic Hamiltonian, the renormalization group method provides an effective theory for low-energy scales by integrating out high-energy degrees of freedom, reducing the UV cutoff $\Lambda = \Lambda_0 e^{-\ell}$. The starting point of this approach is the many-body partition function

$$\mathcal{Z} = \int \sum_{\gamma} \mathcal{D}\bar{\Psi}_{\gamma} \mathcal{D}\Psi_{\gamma} e^{S\{\bar{\Psi}_{\gamma}, \Psi_{\gamma}\}} \ , \tag{2.1}$$

where Ψ, $\bar{\Psi}$ are Grassmann fields with auxiliary index γ, including frequency, momentum, orbital and spin variables. These fields are divided into high ($\Psi_{>}$) and low ($\Psi_{<}$) energy modes depending on whether their energies are higher or lower than the energy cut-off Λ, and the action can then be written as

$$S\{\Psi_<, \Psi_>\} = S_0\{\Psi_<\} + S_0\{\Psi_>\} + S_I\{\Psi_<, \Psi_>\} \ , \tag{2.2}$$

where S_0 is the non-interacting quadratic part and S_I contains quartic interaction terms.

The effective low-energy action containing only low-energy modes is obtained by tracing out high-energy modes and is given by

$$S_\Lambda = \ln \int \mathcal{D}\bar{\Psi}_> \mathcal{D}\Psi_> e^{S\{\Psi_<, \Psi_>\}} \ . \tag{2.3}$$

This procedure is carried out in infinitesimal successive steps, $\Lambda \to \Lambda' = \Lambda e^{-d\ell}$. As shown in Fig. 2.1, the recursive steps of integrating out high energy modes result in a serious of effective Hamiltonian at different RG scale ℓ. Back to the formulation of partition function, we have

$$\begin{aligned} \mathcal{Z} &= \int \sum_\gamma \mathcal{D}\bar{\Psi}_\gamma \mathcal{D}\Psi_\gamma e^{S_0\{\Psi_<\}} e^{S_0\{\Psi_>\}} e^{S_I\{\Psi_<, \Psi_>\}} \\ &= \int \mathcal{D}\bar{\Psi}_< \mathcal{D}\Psi_< e^{S_0\{\Psi_<\}} \int \mathcal{D}\bar{\Psi}_> \mathcal{D}\Psi_> e^{S_0\{\Psi_>\}} e^{S_I\{\Psi_<, \Psi_>\}} \qquad (2.4) \\ &= \int \mathcal{D}\bar{\Psi}_< \mathcal{D}\Psi_< e^{S'\{\Psi_<\}} \ . \qquad (2.5) \end{aligned}$$

The effective action S' is given by

$$\begin{aligned} e^{S'\{\Psi_<\}} &= e^{S_0\{\Psi_<\}} \int \mathcal{D}\bar{\Psi}_> \mathcal{D}\Psi_> e^{S_0\{\Psi_>\}} e^{S_I\{\Psi_<, \Psi_>\}} \\ &= e^{S_0\{\Psi_<\}} \frac{\int \mathcal{D}\bar{\Psi}_> \mathcal{D}\Psi_> e^{S_0\{\Psi_>\}} e^{S_I\{\Psi_<, \Psi_>\}}}{\int \mathcal{D}\bar{\Psi}_> \mathcal{D}\Psi_> e^{S_0\{\Psi_>\}}} \int \mathcal{D}\bar{\Psi}_> \mathcal{D}\Psi_> e^{S_0\{\Psi_>\}} \\ &= e^{S_0\{\Psi_<\}} \langle e^{S_I\{\Psi_<, \Psi_>\}} \rangle_{0>} \qquad (2.6) \end{aligned}$$

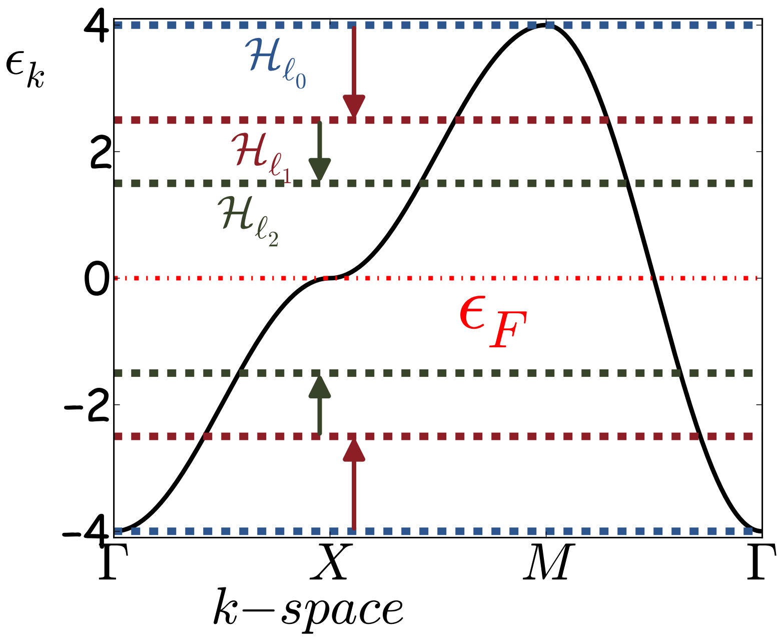

Figure 2.1: The recursive steps of integrating out high energy modes push the cut-off Λ_ℓ toward Fermi level ϵ_F. This systematic procedure results in flow of effective Hamiltonian $\mathcal{H}_{\ell_0} \to \mathcal{H}_{\ell_1} \to \mathcal{H}_{\ell_2}$

, where the constant term ($Z_{0>} = \int [d\Psi_>] e^{S_0\{\Psi_>\}}$) is drop in last line. We rewrite above equation into

$$e^{S'\{\Psi_<\}} = e^{S_0\{\Psi_<\}} \langle e^{S_I\{\Psi_<,\Psi_>\}} \rangle_{0>} = e^{S_0 + \delta S'} \ . \tag{2.7}$$

Then we expand it by means of cumulant expansion to get

$$\delta S' = \langle \delta S \rangle + \frac{1}{2}(\langle \delta S^2 \rangle - \langle \delta S \rangle^2) + \cdots\cdots \tag{2.8}$$

, where the δS is linear in four-point vertex (U).

Here, we present an example with $SU(2)$ symmetry [6, 7]. We calculate the corrections to the interaction vertices to one-loop level [6]. During this RG process, we do not assume any prior order parameters. Both particle-particle (pp) diagram in Fig. 2.2b

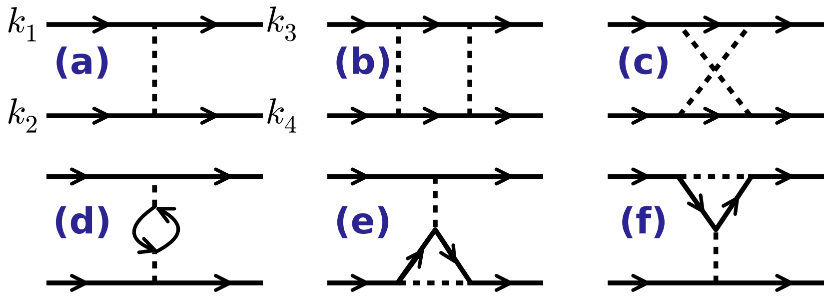

Figure 2.2: (a) A four-point vertex function $U(\boldsymbol{k}_1, \boldsymbol{k}_2, \boldsymbol{k}_3, \boldsymbol{k}_4 = \boldsymbol{k}_1 + \boldsymbol{k}_2 - \boldsymbol{k}_3)$. (b)-(f) One-loop diagrams that contribute to the renormalization of a four-point vertex.

and particle-hole (ph) diagrams in Figs. 2.2c-2.2f are included. Therefore, entire process is unbiased to any order state. We show all one-loop Feynman diagrams in Figs. 2.2b-2.2f, and corresponding RG equation is given by following

$$\begin{aligned}\partial_\ell U(\ell) = \beta_\ell\{U\} &= \beta_{\text{pp}}\{U,U\} + 2\beta_{\text{ph}}\{U,U\} \\ &\quad -\beta_{\text{ph}}\{U,XU\} - \beta_{\text{ph}}\{XU,U\} - X\beta_{\text{ph}}\{XU,XU\}\ . \qquad (2.9)\end{aligned}$$

The function β is a vertex object and a bilinear functional of four-point vertex at different RG scale, $U(\ell)$. The operator X acting on a four-point vertex object exchange its indices, saying $XF(1,2,3,4) = F(2,1,3,4)$. β_{pp} is the particle-particle part of beta function, diagrammatically shown in Fig. 2.2b, and it is given by

$$\beta_{\text{pp}}\{U,U\} = \Xi\{U,U\} + \Xi\{XU,XU\} \qquad (2.10)$$

$2\beta_{\text{ph}}\{U,U\}$ is the particle-hole diagram with Fermi bubble in Fig. 2.2d, and it is worthy to mention that -2 from Fermi bubble is included here. The particle-particle beta function is given by

$$\beta_{\text{ph}}\{U_1,U_2\} = \Pi\{U_1,U_2\} + \mathcal{T}\Pi\{U_1,U_2\} \qquad (2.11)$$

, with the time inversion operator $\mathcal{T}F(1,2,3,4) = F(3,4,1,2)$. Both Ξ and Π four-point functions are the on-shell integrals of particle-particle and particle-hole diagrams. More explicitly, it can be written in integral form with two fermion propagators (also known as Green's function) as following

$$\Xi\{U,U\}(K_1,K_2,K_3,K_4) = \frac{-\Lambda_\ell}{(2\pi)^2}\sum_{\nu=\pm}\int \frac{ds_\nu}{v_\nu}\Theta(|\epsilon_{\boldsymbol{k}_\nu-\boldsymbol{q}_{\rm pp}}| - \Lambda_\ell) \times \tag{2.12}$$

$$T\sum_{\omega_n} G_\ell(K_{(\nu)})G_{\ell_{\rm pp}}(-K_{(\nu)}+Q_{\rm pp}) \times U(K_1,K_2,K_{(\nu)},\ell_{\rm pp})U(K_3,K_4,K_{(\nu)},\ell_{\rm pp})$$

$$\Pi\{U_1,U_2\}(K_1,K_2,K_3,K_4) = \frac{-\Lambda_\ell}{(2\pi)^2}\sum_{\nu=\pm}\int \frac{ds_\nu}{v_\nu}\Theta(|\epsilon_{\boldsymbol{k}_\nu+\boldsymbol{q}_{\rm ph}}| - \Lambda_\ell) \times \tag{2.13}$$

$$T\sum_{\omega_n} G_\ell(K_{(\nu)})G_{\ell_{\rm ph}}(-K_{(\nu)}+Q_{\rm ph}) \times U_1(K_1,K_{(\nu)},K_3,\ell_{\rm ph})U_2(K_4,K_{(\nu)},K_2,\ell_{\rm ph})\ .$$

The summation over index $\nu = \pm$ is over inner shell (below Fermi level) and outer shell (above Fermi level). We sketch it in Fig. 2.1. The integral is along a constant energy curve $\epsilon = \nu\Lambda$, and v_ν are on-shell velocities. The symbol K_ν contains momentum ($\boldsymbol{k}$), frequency (ω_n), and orbitals (o) etc.. The quantity inside those propagators are

$$Q_{\rm pp} = (\boldsymbol{q}_{\rm pp}, \omega_{n,{\rm pp}}, o_{\boldsymbol{q}}) = K_1 + K_2 \tag{2.14}$$

$$Q_{\rm ph} = (\boldsymbol{q}_{\rm ph}, \omega_{n,{\rm ph}}, o_{\boldsymbol{q}}) = K_1 - K_3\ . \tag{2.15}$$

Next, we are going to neglect the self-energy correction since it is just a constant which can be absorbed into chemical potential in one-loop manner [6]. Thus, we can use bare Fermi propagator in above equations: $G_\ell \to G_0 \equiv (i\omega - \epsilon_{\boldsymbol{k}})^{-1}$. According to Shankar's argument at tree level [3], marginal four-point vertex is independent of the magnitude of momentum and frequency. Therefore, we can simplify two vertices in terms of angles, instead of auxiliary indecies:

$$U(K_1,K_2,K_3,\ell) \to U(\theta_1,\theta_2,\theta_3,\ell),\ \omega_{1,2,3,4} = 0,\ \text{and } 1,2,3,4 \text{ on Fermi surface.} \tag{2.16}$$

Next, we assume zero temperature ($T \to 0$), and perform Matsubara summation [6] on Eq. 2.12. In order to solve the RG flow equations numerically, we discretize the Fermi surfaces[6, 5] into finite number of patches and label the interaction vertices in terms of patch-indices, instead of angles: $U(\theta_1, \theta_2, \theta_3, \ell) \to U(i_1, i_2, i_3, \ell)$.

For the multi-species system we consider in following chapters, each solid line in these diagrams also carries a spin and a species index. If the Hamiltonian has $SU(2)$ symmetry for each species, it is enough to calculate only vertices in which fermions with antiparallel spins interact, as vertices involving fermions with the same spin can be obtained from these by imposing $SU(2)$ symmetry[6]. Depending on the species indices, we have intra-species interaction vertices for each species and also inter-species vertices. On the other hand, if system Hamiltonian also has global $U(1)$ symmetry and interactions are density-density type, to each fermion annihilated (incoming fermion line in Fig. 2.2) corresponds a fermion with the same spin and species indices being created (outgoing line). Momentum conservation requires $\boldsymbol{k}_1 + \boldsymbol{k}_2 = \boldsymbol{k}_3 + \boldsymbol{k}_4$ in every vertex. Also, the species indices appear as a pair with the same spin; this follows from the density-density nature of the inter-species interaction in the Hamiltonian.

2.2 RG Flow Analysis

After carrying out the one-loop RG calculations, we obtain the flow of four-point vertices in terms of the RG scale ℓ, and three independent momenta, $U(\boldsymbol{k}_1, \boldsymbol{k}_2, \boldsymbol{k}_3, \ell)$. The momenta are discretized in the numerical implementation but we describe here the general analysis in terms of momenta. The signature for the occurrence of an instability of the Fermi liquid state in the RG approach is the development of run-away flows. In order to determine the dominant instability, we look at the quartic interaction terms in the effective action in the form $\sum_{\boldsymbol{k},\boldsymbol{p}} \mathcal{V}^{(\ell)}_{\mathrm{op}}(\boldsymbol{k},\boldsymbol{p})\hat{\mathcal{O}}^{\dagger}_{\boldsymbol{k}}\hat{\mathcal{O}}_{\boldsymbol{p}}$, with $\hat{\mathcal{O}}_{\boldsymbol{k}}$ being a term bilinear in the fermion fields and corresponding to the order parameter (OP) of pairing (SC), charge density wave (CDW), spin-density wave (SDW), ferromagnetism (FM) or Pomeranchuk (PI) instabilities[6, 14]. Detail definitions of order parameters are given in appendix. The choice of order parameters depends on different symmetry property of Hamiltonian. We discuss three different types of symmetry in the following.

2.2.1 $U(1)$ symmetry

The straightforward case is the spinless fermion, which only has $U(1)$ symmetry. The order parameters we can have are spin-triplet SC, CDW and PI. The corresponding matrices are related to U by

$$\begin{aligned}
\mathcal{V}^{(\ell)}_{SC}(\boldsymbol{k},\boldsymbol{p}) &= U(\boldsymbol{k},-\boldsymbol{k},\boldsymbol{p},-\boldsymbol{p},\ell) && (2.17)\\
\mathcal{V}^{(\ell)}_{CDW}(\boldsymbol{k},\boldsymbol{p}) &= U(\boldsymbol{k},\boldsymbol{p},\bar{\boldsymbol{k}},\bar{\boldsymbol{p}},\ell) && (2.18)\\
\mathcal{V}^{(\ell)}_{PI}(\boldsymbol{k},\boldsymbol{p}) &= U(\boldsymbol{k},\boldsymbol{p},\boldsymbol{k},\boldsymbol{p},\ell)\ , && (2.19)
\end{aligned}$$

where $\bar{\boldsymbol{k}} = \boldsymbol{k}+\boldsymbol{Q}$, $\bar{\boldsymbol{p}} = \boldsymbol{p}+Q$, and $\boldsymbol{Q}$ is the nesting vector at particular filling, and the momenta, $\boldsymbol{k}$, $\boldsymbol{p}$, lie on Fermi surface.

2.2.2 $SU(2)$ symmetry

If system has $SU(2)$ symmetry, we can write most general interaction form into spin-spin and charge-charge, or singlet-singlet and triplet-triplet interactions. The corresponding matrices are related to $U = U_{\sigma\bar{\sigma}}$ by

$$\begin{aligned}
\mathcal{V}^{(\ell)}_{SC_{s(t_0)}}(\boldsymbol{k},\boldsymbol{p}) &= \frac{1}{2}\left[U(\boldsymbol{k},-\boldsymbol{k},\boldsymbol{p},-\boldsymbol{p},\ell) \pm U(-\boldsymbol{k},\boldsymbol{k},\boldsymbol{p},-\boldsymbol{p},\ell)\right] && (2.20)\\
\mathcal{V}^{(\ell)}_{SDW}(\boldsymbol{k},\boldsymbol{p}) &= -U(\boldsymbol{p},\boldsymbol{k},\bar{\boldsymbol{k}},\bar{\boldsymbol{p}},\ell) && (2.21)\\
\mathcal{V}^{(\ell)}_{CDW}(\boldsymbol{k},\boldsymbol{p}) &= 2U(\boldsymbol{k},\boldsymbol{p},\bar{\boldsymbol{k}},\bar{\boldsymbol{p}},\ell) - U(\boldsymbol{p},\boldsymbol{k},\bar{\boldsymbol{k}},\bar{\boldsymbol{p}},\ell) && (2.22)\\
\mathcal{V}^{(\ell)}_{FM}(\boldsymbol{k},\boldsymbol{p}) &= -U(\boldsymbol{p},\boldsymbol{k},\boldsymbol{k},\boldsymbol{p},\ell) && (2.23)\\
\mathcal{V}^{(\ell)}_{PI}(\boldsymbol{k},\boldsymbol{p}) &= 2U(\boldsymbol{k},\boldsymbol{p},\boldsymbol{k},\boldsymbol{p},\ell) - U(\boldsymbol{p},\boldsymbol{k},\boldsymbol{k},\boldsymbol{p},\ell)\ , && (2.24)
\end{aligned}$$

The singlet(triplet) SC instability channel is denoted by $SC_s(SC_{t_0})$, and corresponds to the plus(minus) sign in the right-hand side of the first equation above. In the numerical implementation, each Fermi surface is discretized into patches and $\boldsymbol{k}$, $\boldsymbol{p}$ can be labeled by a discrete patch index that goes from 1 to M(total patch number).

In multi-species system, the couplings $\mathcal{V}^{(\ell)}_{\mathrm{op}}(\boldsymbol{k},\boldsymbol{p})$ contain both intra- and inter-species couplings, depending on whether the momenta $\boldsymbol{k}$ and $\boldsymbol{p}$ are on the same Fermi surface or on different Fermi surfaces, and thus $\boldsymbol{k}$ and $\boldsymbol{p}$ have M values. Explicitly, each $\mathcal{V}$ matrix is block diagonal for intra-species and block off-diagonal for inter-species. For each order parameter channel, we can further diagonalize $\mathcal{V}^{(\ell)}_{\mathrm{op}}(\boldsymbol{k},\boldsymbol{p})$ into

$$\mathcal{V}^{(\ell)}_{\mathrm{op}}(\boldsymbol{k},\boldsymbol{p}) = \sum_{j,oo'} \Delta^{(j)}_{\mathrm{op}}(\ell)\eta_o f^{(j)*}_{\mathrm{op}}(\boldsymbol{k},o,\ell)\eta_{o'} f^{(j)}_{\mathrm{op}}(\boldsymbol{p},o',\ell)\ , \tag{2.25}$$

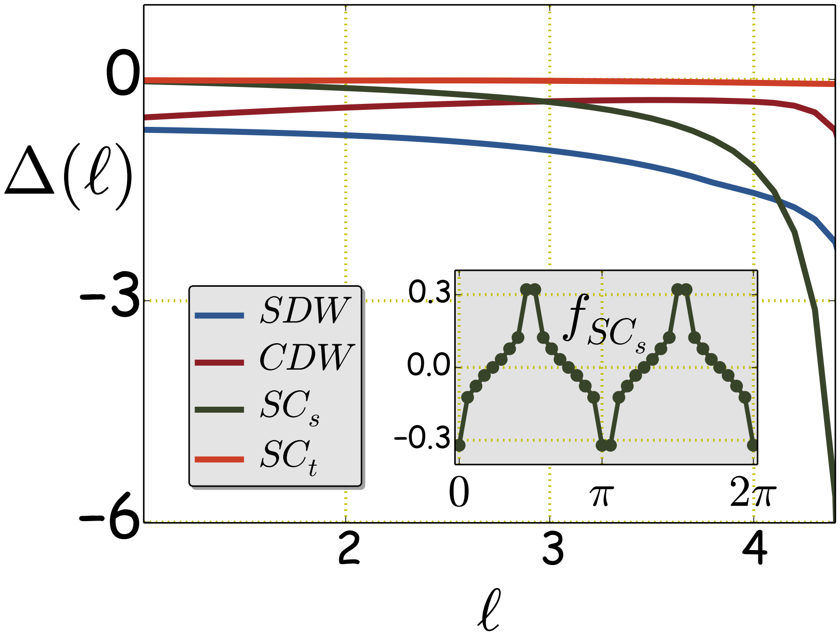

Figure 2.3: An example of RG flows. We only plot the leading eigenvalue in each channels.

with j being a decomposition index, and where now we explicitly indicate the species index o and o' for different types of species. In Fig. 2.3, we show an example of RG flow which determines an instability. The leading instability can be determined by the most negative eigenvalue $w_{\mathrm{op}}^{\mathrm{min}}$ (largest magnitude), and the corresponding symmetry of the instability (s-, p-, and d-wave etc.) is given by the form factor $f_{\mathrm{op}}^{\mathrm{min}}(\boldsymbol{k})$. The sign structure factor $\eta_o = 1(-1)$ stands for in-phase (out-phase) between species on lattice.

2.2.3 Broken $SU(2)$ symmetry

In order to analyze the RG flow in this non-$SU(2)$ symmetry case, we need to derive the instability channels from its original definition, which is shown in appendix. Also, we need to keep spin indices all the time. On the other hand, we still keep global $U(1)$ symmetry.

As a consequence of $SU(2)$ symmetry broken, the spin-spin interactions decompose into longitudinal(SDW_z) and transpose direction(SDW_{xy}). The order parameters in density wave channels are

$$\begin{aligned}
\mathcal{V}^{(\ell)}_{CDW}(\boldsymbol{k},\boldsymbol{p}) &= U_{\uparrow\uparrow}(\boldsymbol{k},\boldsymbol{p},\bar{\boldsymbol{k}},\bar{\boldsymbol{p}},\ell) - U_{\uparrow\uparrow}(\boldsymbol{p},\boldsymbol{k},\bar{\boldsymbol{k}},\bar{\boldsymbol{p}},\ell) + U_{\downarrow\downarrow}(\boldsymbol{k},\boldsymbol{p},\bar{\boldsymbol{k}},\bar{\boldsymbol{p}},\ell) - \\
&\quad U_{\downarrow\downarrow}(\boldsymbol{p},\boldsymbol{k},\bar{\boldsymbol{k}},\bar{\boldsymbol{p}},\ell) + U_{\uparrow\downarrow}(\boldsymbol{k},\boldsymbol{p},\bar{\boldsymbol{k}},\bar{\boldsymbol{p}},\ell) + U_{\downarrow\uparrow}(\boldsymbol{k},\boldsymbol{p},\bar{\boldsymbol{k}},\bar{\boldsymbol{p}},\ell) \qquad (2.26) \\
\mathcal{V}^{(\ell)}_{SDW_z}(\boldsymbol{k},\boldsymbol{p}) &= U_{\uparrow\uparrow}(\boldsymbol{k},\boldsymbol{p},\bar{\boldsymbol{k}},\bar{\boldsymbol{p}},\ell) - U_{\uparrow\uparrow}(\boldsymbol{p},\boldsymbol{k},\bar{\boldsymbol{k}},\bar{\boldsymbol{p}},\ell) + U_{\downarrow\downarrow}(\boldsymbol{k},\boldsymbol{p},\bar{\boldsymbol{k}},\bar{\boldsymbol{p}},\ell) - \\
&\quad U_{\downarrow\downarrow}(\boldsymbol{p},\boldsymbol{k},\bar{\boldsymbol{k}},\bar{\boldsymbol{p}},\ell) - U_{\uparrow\downarrow}(\boldsymbol{k},\boldsymbol{p},\bar{\boldsymbol{k}},\bar{\boldsymbol{p}},\ell) - U_{\downarrow\uparrow}(\boldsymbol{k},\boldsymbol{p},\bar{\boldsymbol{k}},\bar{\boldsymbol{p}},\ell) \qquad (2.27) \\
\mathcal{V}^{(\ell)}_{SDW_{xy}}(\boldsymbol{k},\boldsymbol{p}) &= -U_{\uparrow\downarrow}(\boldsymbol{p},\boldsymbol{k},\bar{\boldsymbol{k}},\bar{\boldsymbol{p}},\ell) = -U_{\downarrow\uparrow}(\boldsymbol{p},\boldsymbol{k},\bar{\boldsymbol{k}},\bar{\boldsymbol{p}},\ell)\ . \qquad (2.28)
\end{aligned}$$

For pairing order parameters, three triplet states(t_0 and $t_\pm$) are no longer degenerate when $SU(2)$ symmetry is broken.

$$\begin{aligned}
\mathcal{V}^{(\ell)}_{SC_s}(\boldsymbol{k},\boldsymbol{p}) &= \frac{1}{4}\left[U_{\uparrow\downarrow}(\boldsymbol{k},-\boldsymbol{k},\boldsymbol{p},-\boldsymbol{p},\ell) + U_{\downarrow\uparrow}(\boldsymbol{k},-\boldsymbol{k},\boldsymbol{p},-\boldsymbol{p},\ell) + \right. \\
&\quad \left. U_{\uparrow\downarrow}(-\boldsymbol{k},\boldsymbol{k},\boldsymbol{p},-\boldsymbol{p},\ell) + U_{\downarrow\uparrow}(-\boldsymbol{k},\boldsymbol{k},\boldsymbol{p},-\boldsymbol{p},\ell)\right] \qquad (2.29) \\
\mathcal{V}^{(\ell)}_{SC_{t0}}(\boldsymbol{k},\boldsymbol{p}) &= \frac{1}{4}\left[U_{\uparrow\downarrow}(\boldsymbol{k},-\boldsymbol{k},\boldsymbol{p},-\boldsymbol{p},\ell) - U_{\downarrow\uparrow}(\boldsymbol{k},-\boldsymbol{k},\boldsymbol{p},-\boldsymbol{p},\ell) + \right. \\
&\quad \left. U_{\uparrow\downarrow}(-\boldsymbol{k},\boldsymbol{k},\boldsymbol{p},-\boldsymbol{p},\ell) - U_{\downarrow\uparrow}(-\boldsymbol{k},\boldsymbol{k},\boldsymbol{p},-\boldsymbol{p},\ell)\right] \qquad (2.30) \\
\mathcal{V}^{(\ell)}_{SC_{t+}}(\boldsymbol{k},\boldsymbol{p}) &= \frac{1}{2}\left[U_{\uparrow\uparrow}(\boldsymbol{k},-\boldsymbol{k},\boldsymbol{p},-\boldsymbol{p},\ell) - U_{\uparrow\uparrow}(-\boldsymbol{k},\boldsymbol{k},\boldsymbol{p},-\boldsymbol{p},\ell)\right] \qquad (2.31) \\
\mathcal{V}^{(\ell)}_{SC_{t-}}(\boldsymbol{k},\boldsymbol{p}) &= \frac{1}{2}\left[U_{\downarrow\downarrow}(\boldsymbol{k},-\boldsymbol{k},\boldsymbol{p},-\boldsymbol{p},\ell) - U_{\downarrow\downarrow}(-\boldsymbol{k},\boldsymbol{k},\boldsymbol{p},-\boldsymbol{p},\ell)\right]\ . \qquad (2.32)
\end{aligned}$$

If we apply the $SU(2)$ symmetry properties that $U_{\sigma\sigma}(\boldsymbol{k}_1,\boldsymbol{k}_2,\boldsymbol{k}_3,\boldsymbol{k}_4) = \frac{1}{2}(U_{\sigma\bar{\sigma}}(\boldsymbol{k}_1,\boldsymbol{k}_2,\boldsymbol{k}_3,\boldsymbol{k}_4) - U_{\sigma\bar{\sigma}}(\boldsymbol{k}_2,\boldsymbol{k}_1,\boldsymbol{k}_3,\boldsymbol{k}_4))$, the above definitions coincide with those definitions in 2.2.2.

Chapter 3

2D Extended Hubbard Model on Square Lattice

3.1 Introduction

An extended Hubbard model is generally employed as a theoretical framework of screened electronic interactions and regarded as a prototypical scenario for rich quantum phases in condensed matter physics [15, 16, 17]. In a one-dimensional chain, for instance, an extended Hubbard model, including an on-site and nearest-neighbor interactions, presents correlated phases associated with the ratio of the two interactions [18, 19]. Recent identification of the bond-charge-density-wave instability between charge and spin density-wave phases, at weak and strong interactions, completes the phase diagram of this model [20, 21, 22, 23, 24, 25]. Meanwhile, in a two-leg ladder, a checkerboard charge-ordered state has been proposed for all fillings between quarter and half, with on-site and nearest-neighbor repulsion [26]. Its application to the coupled quarter-filled ladders with coupling to the lattice has recently been studied [27] to explain the spin gaps in the $\mathrm{NaV_2O_5}$ material [28, 29].

On a two-dimensional lattice, the extended Hubbard model has been considered a paradigmatic model to search for possible unconventional superconducting phases since the discovery of high-temperature superconductivity in the cuprates [30]. Although a nearest-neighbor repulsion between electrons suppresses non-s-wave pairings tendencies [31], it is generally believed that the nesting of the Fermi surface plays a key role in driving unconventional pairing under purely repulsive interactions at weak couplings [18, 32, 33, 7, 34, 35, 36]. In the proximity of density-wave order, for instance, a chiral d-wave state has been found for an extended Hubbard model on both triangular and honeycomb lattices [37, 38, 39]. Furthermore, following the recent experimental realization of a two-dimensional Kagome lattice for ultracold atoms [40], the phase diagram of the extended Hubbard model on a Kagome lattice has been established in the vicinity of van Hove fillings [41]. It was shown that a possible p-wave charge and spin bond order can be triggered in the presence of a nearest-neighbor repulsion for van Hove fillings, then giving way to a f-wave superconducting phase when slightly doped away [39].

It has recently been proposed that under a nearest-neighbor attraction and on-site repulsion a singlet $(p + ip)$-wave pairing emerges on a honeycomb lattice [42]. Along with the result that Majorana fermions can be generated as a zero-energy mode in the excitation spectrum of a half-quantum vortex in a $(p + ip)$-wave superconductor [43], this indicates the possibility of creating Majorana fermions in graphene in the presence of a magnetic field. However, a functional renormalization group study has shown that for a honeycomb structure, the f-wave pairing is preferred and is stabilized by introducing a next-nearest-neighbor attraction [37]. Although triplet p-wave superconductivity has been proposed for an extended Hubbard model on a square lattice for purely repulsive interactions [44, 45], the physics of long-range interactions, with possibly terms leading to competing instabilities, has been studied recently, leading that the existence of p-wave pairing is still an open question [46, 34, 35].

3.2 Model and Formalism

In this chapter, we study the phase diagram of an extended Hubbard model via a functional renormalization group (FRG) approach [3, 5, 6], including on-site U and nearest-neighbor V interactions, on a two-dimensional square lattice. The total Hamiltonian can be written as, $H = H_0 + H_{\text{int}}$, with the non-interacting and interacting parts,

$$H_0 = -t \sum_{\langle ij \rangle, \alpha} \left(c^\dagger_{i\alpha} c_{j\alpha} + \text{H.c.} \right) - \mu \sum_i n_i, \tag{3.1}$$

$$H_{\text{int}} = U \sum_i n_{i\uparrow} n_{i\downarrow} + V \sum_{\langle ij \rangle} n_i n_j, \tag{3.2}$$

respectively, where $\langle ij \rangle$ represents nearest-neighbor pairs of sites, $n_i = n_{i\uparrow} + n_{i\downarrow} = \sum_\alpha c^\dagger_{i\alpha} c_{i\alpha}$ and μ is the chemical potential. Without the nearest-neighbor interaction, the phase diagram in a FRG analysis is well developed in the limit of weak couplings [5]. For on-site attraction, s-wave superconductivity (s-SC) dominates at all fillings except for half-filling. The phase diagram for on-site repulsion, $U = 1$, versus μ is sketched in Fig. 3.1. In the vicinity of half-filling, the spin-density wave (SDW) dominates due to the strong nesting of the Fermi surface. With slight doping, $d_{x^2-y^2}$-SC emerges in a small regime of μ just away from half-filling. When the magnitude of μ is further increased, no instability develops in our analysis, up to the point where we stop the RG flows, at energy cutoffs lower than $10^{-6}t$. Kohn-Luttinger (KL) instability [47] is expected to occur in this regime. Sufficiently away from half-filling, the particle-hole channels can be treated perturbatively, and the RG flows at low energies can be calculated including the particle-particle diagram only [6]. Previous works have found that the $d_{x^2-y^2}$-wave SC phase near half-filling is followed by a d_{xy}-phase upon doping [6, 34, 35], or by a p-wave SC phase that is then followed by a d_{xy}-wave SC phase [44].

3.3 Results

In presence of a nearest-neighbor interaction V, the phase diagram is much richer. We find that d_{xy}- and $(p_x + ip_y)$-wave pairing superconducting states develop. In the proximity of the charge-density-wave (CDW) order, d_{xy}-wave pairing emerges from the CDW instability with $U > 0$ and $V > 0$. When the nesting of the Fermi surface is decreased, a time-reversal symmetry breaking $(p_x + ip_y)$-SC arises from the $d_{x^2-y^2}$-SC with a sufficient large nearest-neighbor attraction. When nesting is completely suppressed, $(p_x + ip_y)$-SC dominates in the whole regime of $U \geq 0$ and $V < 0$, and the d_{xy}-pairing is only triggered with the help of an on-site attraction. Using a symmetry argument, we show that appearance of $(p_x + ip_y)$-SC on a square lattice for $V < 0$ is generic and robust due to the underlaying lattice structure, and can be used to create a zero mode Majorana fermion in the presence of a magnetic field.

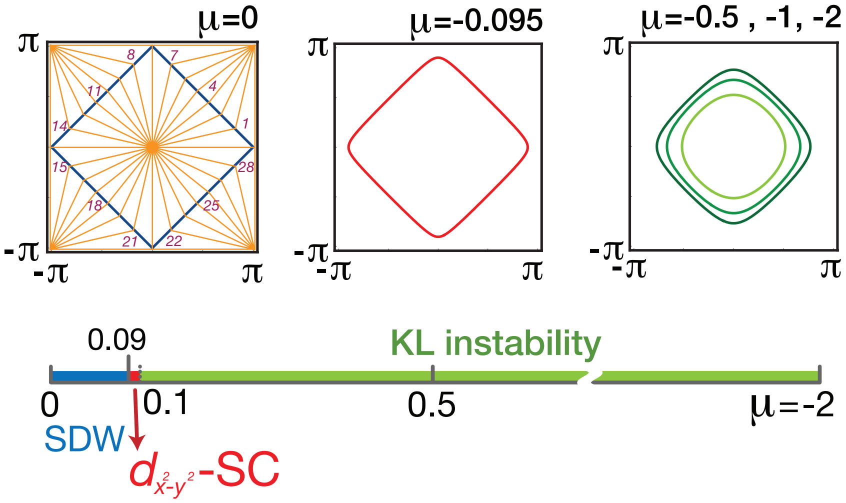

Figure 3.1: Fermi surfaces of a square lattice with nearest-neighbor hopping, at different chemical potentials μ (in units of t). Below, the phase diagram versus μ for $U = 1$ and $V = 0$. The Fermi surface patches used in this study are illustrated in the Fermi surface at $\mu = 0$.

3.3.1 At and near half filling

Starting with the bare Hamiltonian, Eq. (3.2), we follow standard FRG procedure integrating out high-energy modes, decreasing the energy cut-off Λ. The four-fermion terms in the resulting effective Hamiltonian are written in the form

$$g(\boldsymbol{k}_1, \boldsymbol{k}_2, \boldsymbol{k}_3, \Lambda)\psi^\dagger_\alpha(\boldsymbol{k}_3)\psi^\dagger_\beta(\boldsymbol{k}_1 + \boldsymbol{k}_2 - \boldsymbol{k}_3)\psi_\beta(\boldsymbol{k}_2)\psi_\alpha(\boldsymbol{k}_1) \tag{3.3}$$

, in momentum space, with $\boldsymbol{k} = (k_x, k_y)$ and spin indices α, β. In previous studies, the RG equations for models with $SU(2)$ and $U(1)$ symmetries have been systematically studied by Fermi surface discrete patch-approximation [5]. In this chapter, to preserve the particle-hole symmetry of the non-interacting Hamiltonian at half-filling, all phase diagrams are obtained by the configuration of the Fermi surface patches illustrated in Fig. 3.1. By integrating out

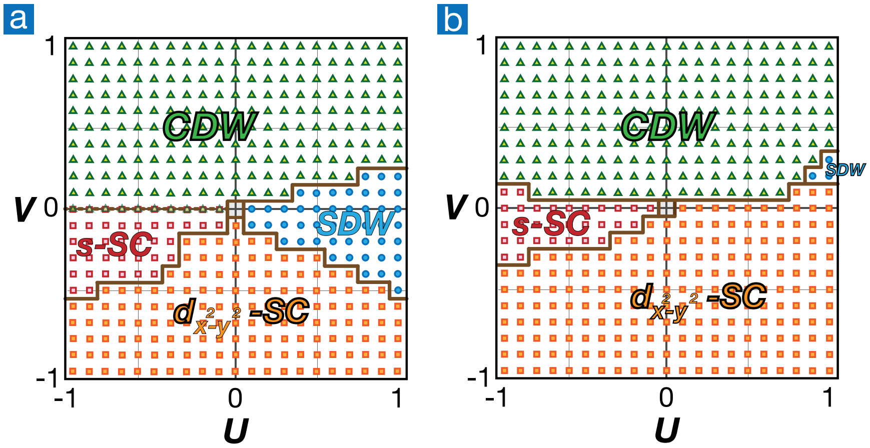

Figure 3.2: The phase diagram (a) at half-filling $\mu = 0$, (b) at $\mu = -0.095$, parameterized by on-site U and nearest-neighbor interaction V. The interaction terms U and V are in units of t throughout this chapter.

high energy degrees of freedom and neglecting self-energy corrections, the RG flows of all couplings versus the decreasing running energy cutoff Λ are computed. Before the system flows into the strong couplings regime, we truncate the RG process when the absolute magnitude of one of the couplings reaches $\sim 30t$.

To determine the dominant instability, we decompose specific four-fermion interaction terms in the Hamiltonian as $\sum_{\boldsymbol{k},\boldsymbol{p}} \mathcal{V}_{\mathrm{op}}(\boldsymbol{k},\boldsymbol{p},\Lambda)\hat{\mathcal{O}}_{\boldsymbol{k}}^{\dagger}\hat{\mathcal{O}}_{\boldsymbol{p}}$, with $\hat{\mathcal{O}}_{\boldsymbol{k}}$ a bi-fermion operator for the order parameter (op) of SC, CDW, SDW or Pomeranchuk instability. Then, for a given order parameter channel, we further decompose, $\mathcal{V}_{\mathrm{op}}(\boldsymbol{k},\boldsymbol{p},\Lambda) = \sum_i w_{\mathrm{op}}^{i}(\Lambda) f_{\mathrm{op}}^{i*}(\boldsymbol{k},\Lambda) f_{\mathrm{op}}^{i}(\boldsymbol{p},\Lambda)$, in normal modes, with i a symmetry decomposition index. The leading instability can be determined by the most minimum eigenvalue $w_{\mathrm{op}}^{\min}(\Lambda)$ (largest magnitude), and the corresponding symmetry of the instability is given by the form factor $f_{\mathrm{op}}^{\min}(\boldsymbol{k})$ [6, 33].

At half-filling, the phase diagram has been studied extensively by several methods [48, 49, 50]. In our FRG analysis, we include the regime of negative interactions and obtain the phase diagram in Fig. 3.2a, parameterized by on-site interaction U and nearest-neighbor interaction V (in unit of t). The phase boundary between SDW and CDW is at $U \simeq 4V$ for $U, V > 0$, consistent with known results from previous studies. For the line of $V = 0$ and $U < 0$, we find that CDW and s-SC are degenerate, also in agreement with results in the literature [50]. However, the degeneracy is delicate and broken by introduction of a nearest-neighbor interaction: a slight nearest-neighbor attraction drives the system to a s-SC instability, instead of a CDW instability.

We also find that for a sufficiently large nearest-neighbor attraction, a $d_{x^2-y^2}$-SC is triggered, even dominant over the s-SC in the regime of $U < 0$. This d-wave pairing is linked with the nesting of the Fermi surface. In other words, if the nesting effect is suppressed, the s-SC is the dominant instability for a generic Fermi surface in the regime of $U < 0$. Furthermore, without nesting effects, a p-wave, with lower angular momenta than d-wave, will eventually dominate in the regime of $V < 0$ and $U > 0$. However, negative V combined with nesting, leads to $d_{x^2-y^2}$-SC.

By slightly doping away the half-filling, the $d_{x^2-y^2}$-SC overcomes the spin-density-wave instability that dominates for on-site repulsion. The phase diagram parameterized by U and V is illustrated in Fig. 3.2b. The SDW is suppressed to the small regime between CDW and $d_{x^2-y^2}$-SC in the phase diagram. The degenerate line, $U < 0$ and $V = 0$, mentioned above, is dominated by s-SC instability since the Fermi surface is not perfectly nested. However, the CDW is still dominant in the overall regime of $V > 0$.

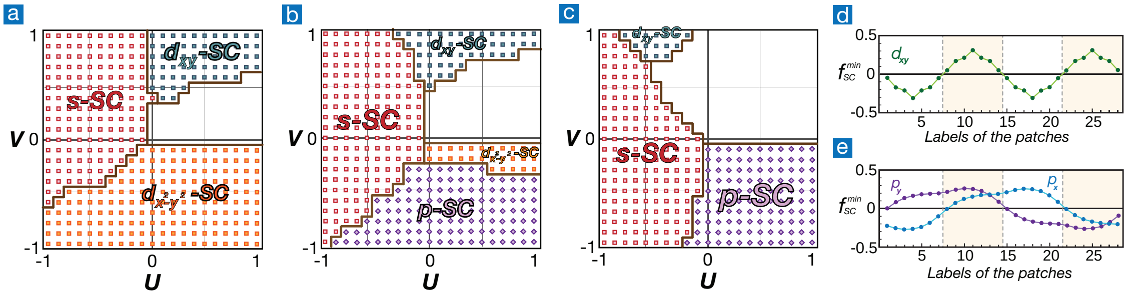

Figure 3.3: Phase diagrams for (a) $\mu = -0.5$, (b) $\mu = -1$ and (c) $\mu = -2$, parameterized by U and V. The transparent regime means no instability is found before we stop the RG process, at which point the energy cutoff is lower than $10^{-6}t$. Form factors obtained from decoupling of pairing channels into bi-fermions during the FRG flows are illustrated for (d) d_{xy}-wave (e) $(p_x + ip_y)$-wave pairings.

3.3.2 Doped systems

Here, we increase doping, decreasing nesting of the until the density-wave instability no longer occurs. Then, as shown as Fig. 3.3a, the d_{xy}-wave SC arises from the CDW instability in the regime of $V > 0$ and $U \geq 0$. The form factors of the d_{xy}-SC in our FRG analysis is plotted in Fig. 3.3d. Although the d_{xy}-SC phase has been proposed for the purely repulsive models [44, 46, 34, 35], the d_{xy}-SC instability we find develops only with an appropriate nearest-neighbor repulsion and also tied with the proximity to nesting of the Fermi surface. It is only when nesting is barely suppressed so that CDW is no longer dominant, but CDW fluctuations are still expected to be strong, that this d_{xy}-SC phase emerges.

As compared with the phase diagram at $\mu = -0.5$ in Fig. 3.3a, the d_{xy}-SC instability moves to the region of larger positive V or negative U when doping is increased, for $\mu = -1$, as shown in Fig. 3.3b. By looking at the RG flows of different couplings, we notice that the different behavior for the two fillings, $\mu = -0.5$ and $\mu = -1$, are mainly coming from the effect of the nesting vertices, that is, couplings $g(\boldsymbol{k}_1, \boldsymbol{k}_2, \boldsymbol{k}_3, \boldsymbol{k}_4)$ with $\boldsymbol{k}_1 + \boldsymbol{k}_2 - \boldsymbol{k}_3 - \boldsymbol{k}_4 = (0, 2\pi)$ or $(2\pi, 0)$ or $(2\pi, 2\pi)$. For $\mu = -1$, there are fewer nesting vertices flowing into large values as compared with the $\mu = -0.5$ case. Without the benefit of nesting vertices, the instability of d_{xy}- and $d_{x^2-y^2}$-SC are suppressed and eventually do not develop by the time we stop the RG flow. As a consequence, when the nesting is completely destroyed, in heavily doped cases, there is no instability found for purely repulsive interactions ($U > 0$ and $V > 0$), as shown in Fig. 3.3c.

The triplet p-SC phase tells an opposite story. In the regime of $V < 0$, under the influence of Fermi surface nesting, $d_{x^2-y^2}$-SC is dominant, as shown as Fig. 3.3a. However, decreasing nesting suppresses the d-wave pairing and the p-SC emerges for large nearest-neighbor attraction, as shown in Fig. 3.3b. When the nesting is no longer present at all, p-SC dominates the regime of $V < 0$ and $U \geq 0$, as illustrated as Fig. 3.3c. The emergence of a triplet p-SC has a clear physical picture in a square lattice. In the presence of a nearest-neighbor attraction $V < 0$, electronic pairings are triggered. To lower energy, a s-wave pairing with the lowest angular momenta would be favored. However, an on-site repulsion suppresses the s-wave pairing so that p-wave, with the second lowest angular momenta, is preferred.

Furthermore, the four-fold symmetry on a square lattice also indicates that the p_x- and p_y-wave instability channels must be degenerate. The degeneracy of two p-wave superconducting instabilities is indeed found in our FRG results and the associated form factors are plotted in Fig. 3.3e. Since the p_x- and p_y-wave superconducting states are degenerate, the gap functions will be given as a linear combination of the two order parameters. By constructing the gap function as $\Delta_{\boldsymbol{k}} = \Delta_{p_x}(\boldsymbol{k}) + v\Delta_{p_y}(\boldsymbol{k})$ with the complex coefficient v containing a possible relative phase, the condensation energy in the standard BCS equation is obtained by the difference in energy between the superconducting and normal states, and is given by

$$\Delta E = E_{\mathrm{SC}} - E_{\mathrm{N}} = 2 \sum_{|\boldsymbol{k}|>k_F} \left[\epsilon_{\boldsymbol{k}} - \frac{2\epsilon_{\boldsymbol{k}}^2 + |\Delta_{\boldsymbol{k}}|^2}{2\sqrt{\epsilon_{\boldsymbol{k}}^2 + |\Delta_{\boldsymbol{k}}|^2}} \right], \tag{3.4}$$

where $\epsilon_{\boldsymbol{k}}$ is the dispersion relation of the non-interacting Hamiltonian. The second term of Eq. (3.4) is maximized when v is purely imaginary, hence the time-reversal breaking pairing symmetry $p_x + ip_y$ is the energetically favored one [38, 39, 51, 52]. One can also preform the Ginzburg-Landau free energy analysis to verify that $p_x + ip_y$ is preferred in energetics [53]. Physically this is reasonable, since this choice of the phase guarantees that a gap forms everywhere along the Fermi surface, lowering the ground-state energy.

3.4 Summary

In atomic Bose-Fermi mixtures, an effective attraction between fermions can be mediated by fluctuations of the Bose-Einstein condensate of the bosons [54, 55, 56]. In the presence of the mediated long-range attraction, the $p_x + ip_y$ wave superconducting state has been proposed in these systems [55]. However, the mechanism discussed here puts some constraint for the emergence of the $p_x + ip_y$-SC phase: in order to develop the $p_x + ip_y$-SC, long-range attraction and on-site repulsion is needed, as well as low density of fermions to avoid nesting of the Fermi surface, while large enough densities such that the Fermi energy is a large scale ($t > U, V$) to justify the validity of FRG results. Another possible way to manifest a mediated attraction is through another species of fermions in a Fermi-Fermi atom mixture [57]. By introducing an inter-species interaction in Fermi-Fermi mixtures, an effective interaction for one species of fermions can be obtained by tracing out the other species. This can be justified, for example, if the one of the species has a much smaller effective mass than the other. In this case, the mediated long-range interaction is found to decay rather rapidly and can be approximated by an effective on-site and nearest-neighbor interactions. By tracing out one species with low electronic density, an effective nearest-neighbor attraction can be obtained. Together with a bare hard-core on-site repulsion, it may provide the required conditions for the creation of the time-reversal breaking $p_x + ip_y$-wave pairing.

In conclusion, we study the phase diagram of an extended Hubbard model, including a on-site U and nearest-neighbor V interactions, on a two-dimensional square lattice. In the proximity of charge-density-wave order, the d_{xy}-SC overcomes the CDW, dominating in the regime of $U > 0$ and $V > 0$, from our FRG analysis. Accompanying the destruction of Fermi surface nesting, a time-reversal breaking $(p_x + ip_y)$-wave superconducting state arises in the regime of $V < 0$. Our results indicates that, without nesting, the $(p_x + ip_y)$-SC on a square lattice under a nearest-neighbor attraction is the generic behavior due to the underlaying lattice structure, and can be used to create a zero mode Majorana fermion in the presence of a magnetic field.

Chapter 4

Spin-Imbalanced Fermi-Fermi Mixture

4.1 Introduction

Experiments with ultra-cold atoms have realized mixtures of two different species of fermionic atoms with different densities, including mixtures of cold lithium atoms (^{6}Li) with different populations for two different hyperfine states [10, 58, 59, 11, 60, 61, 62]. Fermionic systems with imbalanced spin populations have been studied in electronic materials, such as magnetic-field-induced organic superconductors [63, 64]. Mixtures of different species of fermions with unequal populations have also been considered in the study of quark matter [65]. With the rapid experimental advances in the field of cold-atom physics, these systems have the advantage of a great degree of tunability and control of inter-particle interactions, dimensionality, confinement, as well as a number of pseudo-spin species. Imbalanced mixtures of cold fermionic atoms have attracted great interest due to their possible rich phase diagram [62]. Several phases have been observed experimentally [11, 62], such as imbalanced superfluid phase, phase separation, and normal Fermi liquid behavior. Also, the Larkin-Ovchinnikov-Fulde-Ferrel (LOFF) state [66, 67], which involves Cooper pairs with finite center-of-mass momentum, and breached pair [68, 69, 70, 71] state with zero center-of-mass momentum, could be possible phases in special regions of the phase diagram [72]. In addition, there are studies of p-wave triplet pairing, caused by effective attractive intra-species interaction, proposed for strongly imbalanced cases in two [73] and in three [74, 75] dimensions. In addition to being cooled and trapped, fermionic atoms and mixtures can now also be loaded onto optical lattices [76, 77] where the interaction and the hopping strengths can be tuned, and effects of their interplay with lattice geometry and dimensionality can be probed.

We consider a two-component mixture of fermionic atoms with imbalanced populations on a two-dimensional square lattice at weak-coupling region. It is well known that the presence of a lattice can provide interesting strong correlation effects, such as spin density wave (SDW) and charge density wave (CDW) phases for fermions on a two-dimensional (2D) square lattice at half-filling. Extensive studies can be found in the literature for the case of balanced, $SU(2)$-symmetric fermions, such as the Hubbard model [8] in various lattice geometries and fillings [3, 5, 6, 51]. Due to nesting of the Fermi surface (FS), SDW is the dominant instability for the repulsive Hubbard model on a 2D square lattice at half-filling, followed by $d_{x^2-y^2}$-wave superconductivity when the system is doped away from half-filling. [5, 6] When nesting is completely destroyed by doping, the system becomes a normal Fermi liquid, aside from Kohn-Luttinger instabilities [47] at extremely low temperatures. However, when the spin populations are unequal and SU(2) symmetry is broken, both the SDW and the singlet pairing will eventually be precluded due to the mismatch of the FS for the up- and down-spin fermions at strong population imbalance. As the Fermi surfaces become increasingly mismatched, the system is expected to be dominated by other instabilities or becomes a two species Fermi liquid. If the interspecies interaction is initially repulsive, one expects to find SDW phase near the balanced case [78, 79, 80], switching to other and potentially richer correlated behavior as the polarization increases. Here, we study this behavior using a weak-coupling functional renormalization group (FRG) method, [3, 5, 6] which is able to treat different instabilities on an equal footing. We obtain the phase diagram for this system, focusing on the case where the majority species stays close to half-filling and the density of the minority species is varied. The phase diagram (Fig. 4.1) contains several new phases, including a stripe-CDW phase and triplet pairing phases for both species. From our FRG study, we also obtain estimates for the critical temperature for the different instabilities.

For a microscopic interaction which is on-site, there is no bare intra-species interaction due to Pauli exclusion principle, but an effective long-range interaction can be induced via scattering between species. Previous studies [73, 74, 75] have considered such mediated interactions for mixtures of fermion gases (no lattice) with imbalanced populations, finding an attractive effective intra-species pairing interaction, leading to p-wave pairing of the majority species. In this study, we consider the effects of the interplay of interaction, population imbalance, and lattice effects. We show that lattice effects in particular, not only lead to a much richer phase diagram than that of an imbalanced mixture of fermionic gases, but also with a much higher transition temperature, even at weak interaction couplings, therefore more easily accessible to experimental observation. Unlike Bose-Fermi mixtures [54, 55, 81, 82], where different pairing and density wave states for the fermions originate from attractive interactions mediated by quantum fluctuations of the boson condensate, in the fermion mixture considered here, both species have screening effects from each other, and the low energy physics depends on the interplay between initial interspecies interaction, induced intra-species interaction, the FS geometry of each species, and their mismatch due to imbalance.

4.2 Model and Formalism

We consider a one-band Hubbard model for each species ($\sigma = \uparrow, \downarrow$) of fermion (with creation operator $c^{\dagger}_{\boldsymbol{k}\sigma}$) on a 2D square lattice, with on-site interspecies interaction U_0. The Hamiltonian can be written as:

$$\mathcal{H} = \sum_{\sigma \boldsymbol{k}} \xi_{\sigma \boldsymbol{k}} c^{\dagger}_{\boldsymbol{k}\sigma} c_{\boldsymbol{k}\sigma} + \frac{U_0}{V} \sum_{\boldsymbol{k}\boldsymbol{k}'\boldsymbol{q}} c^{\dagger}_{\boldsymbol{k}+\boldsymbol{q}\uparrow} c^{\dagger}_{\boldsymbol{k}'-\boldsymbol{q}\downarrow} c_{\boldsymbol{k}'\downarrow} c_{\boldsymbol{k}\uparrow} \tag{4.1}$$

, where $\xi_{\sigma \boldsymbol{k}} = -2t_{\sigma}(\cos k_x + \cos k_y) + \mu_{\sigma}$ and V is the volume of the system (hereafter set to be equal to 1). The different chemical potentials μ_{σ} determine the densities and the hopping amplitude t_{σ} can be tuned by the optical lattices. In this work, we only consider the case $t_{\uparrow} = t_{\downarrow} = t$, and weak repulsive interspecies interaction ($U_0 > 0$).

4.3 Results

4.3.1 Nearly balanced

In order to maximize lattice effects, we focus on the case where the majority species is at or close to half-filling, $\mu_\uparrow \sim 0$, and we vary $\mu_\downarrow$. Phase diagrams are shown in Fig. 4.1. When the system is balanced ($\mu_\uparrow = \mu_\downarrow = 0$), SDW is the dominant instability (RG flows shown in Fig. 4.2(a)). With increasing $\mu_\downarrow$, the SDW$_z$ order persists for the nearly balanced region (Fig. 4.1), but the critical temperature T_c decreases. This result agrees with previous studies [78] showing that antiferromagnetic order is suppressed by increasing imbalance (i.e. $\Delta\mu$).

4.3.2 Weak imbalance

As the minority density is further decreased away from half-filling, some inter-species vertices involving nesting vectors, such as *Umklapp* processes, are no longer near the FS and are thus suppressed.

However, there are still some non-perfect nesting particle-hole processes with net momentum equal to a reciprocal lattice vector, $(2\pi, 0)$ or $(0, 2\pi)$, which are allowed even under imbalance. An example of such a process, depicted in Fig. 4.2(b), is for a minority fermion to scatter from $\boldsymbol{q} \to \boldsymbol{q} + \mathbf{Q}_2 - \boldsymbol{\delta}$ across two opposite sides of its FS (say along the 45° direction), while a majority fermion scatters from $\boldsymbol{k} \to \boldsymbol{k} + \mathbf{Q}_1 + \boldsymbol{\delta}$ across the other two opposite sides of its FS (say along the 135° direction). With $\mathbf{Q}_1 = (\pi, \pi)$, $\mathbf{Q}_2 = (-\pi, \pi)$, and $\boldsymbol{\delta} = (\delta, \delta)$ accounting for the FS mismatch, the net momentum for this process is $(0, 2\pi)$ and therefore of *Umklapp*-type and allowed by momentum conservation in spite of the imbalance. These vertices can still renormalize significantly under RG flow, and more importantly, they mediate intra-species nesting processes for the majority fermions, which do have a perfectly nested FS, so these mediated processes have the strongest flow. On the other hand, the induced intra-species long-range attraction is maximum at diagonal directions. Due to the partial nesting and intra-species long-range attraction, this leads to a crossover in the RG flows from the SDW_z to a stripe-CDW phase. From a real-space picture, with increasing imbalance, both species also have more empty sites to move around to minimize free energy. Figure 4.2(a) shows the RG flow close to this crossover, where SDW_z and CDW channels are almost degenerate. The CDW channel of both species is doubly degenerate. The order parameters for $\uparrow$ and $\downarrow$ are non-zero on two-opposite sides of the FS (second and fourth quadrants), and zero on the other sides (first and third quadrants), with the situation reversed for the other degenerate channel [Fig. 4.2(c) shows one of the cases[These correspond to stripe charge order in the diagonal direction [83]). This stripe-CDW phase originates from weaker spin fluctuations caused by imbalance in addition to screened intra-species long-range attraction. Since it involves both spin and charge fluctuations, the size of this region and its critical energy scale in phase diagram depend on the filling fraction of both species, shown in Fig. 4.1.

4.3.3 Strong imbalance

As the imbalance becomes stronger, the FS mismatch precludes all nesting processes as well as zero-momentum singlet pairing. Since the induced intra-species interactions are always attractive, the dominant RG flows present another crossover, from CDW stripe phase to triplet p-wave BCS pairing. The triplet pairing is for a single fermion species but it is generated by the initial bare repulsive interspecies interaction, the lattice (FS shape), and the imbalance (FS mismatch). Whether the dominant pairing is for the majority or for the minority species depends on the interplay of these factors. Figure 4.3(a) shows RG flows for three different minority chemical potentials. As $\mu_\downarrow$ increases, the minority pairing channel is dominant at first. This is because the nearly half-filled majority FS provides a large phase space in RG process to mediate and renormalize the minority intra-species BCS vertex. The bubble diagram in Fig. 2.2(d), which contains an internal fermion loop, gives a first nonzero correction to the intra-species vertex from two interspecies vertices, of the form,

$$\partial_\ell U^{(\ell)}_{\sigma\sigma'}(\boldsymbol{k}_1, \boldsymbol{k}_2, \boldsymbol{k}_3) = \left[1 - \frac{1}{2}(1+X)\delta_{\sigma\sigma'}\right]\beta_{ph}\{U_1, U_2\}, \tag{4.2}$$

where X denotes the operation $XF(1,2,3,4) = F(2,1,3,4)$ and $\beta_{ph}\{U_1, U_2\} = \Pi\{U_1, U_2\} + \mathcal{T}\Pi\{U_1, U_2\}$, with $\mathcal{T}F(1,2,3,4) = F(3,4,1,2)$ the time-reversal operator and

$$\Pi\{U_1, U_2\} = \sum_{\boldsymbol{q},\alpha} B_{ph}(\boldsymbol{k}_1, \boldsymbol{k}_3, \boldsymbol{q}) U_{\sigma\alpha}(\boldsymbol{k}_1, \boldsymbol{q}, \boldsymbol{k}_3) U_{\sigma'\alpha}(\boldsymbol{k}_4, \boldsymbol{q}, \boldsymbol{k}_2) \tag{4.3}$$

where B_{ph} is an integral over an angular sector. [6] From Eq. (4.3), the induced intra-species BCS vertex comes from integrating out two interspecies interactions. For example, in Fig. 4.3(b), integrating pairs of solid and dashed lines, which represent two interspecies vertices, results in an intra-species BCS vertex, $U_{\downarrow\downarrow}(\boldsymbol{k}, -\boldsymbol{k}, \boldsymbol{k}', -\boldsymbol{k}')$. Because the FS of the majority species is flat, there will be more renormalization corrections to intra-species interaction between minority species at first. As shown in Fig. 4.3(c), the momentum $\boldsymbol{q}$ at fixed magnitude can be translated anywhere along that branch of the FS. Figure 4.1 shows that the critical temperature(a.u.) for minority pairing decreases monotonically with increasing polarization, because the phase space of induced minority intra-species pairing becomes smaller. The same effect is observed for the majority p-wave pairing channel, which is the sub-leading channel. However, the induced BCS vertex of majority species couples to its own nesting channel [$\boldsymbol{k}$ and $\boldsymbol{k}'$, for example, are connected by a nesting vector in Fig. 4.3(b)]. Although the initial mediated majority intra-species pairing interaction is smaller than that for minority species, as discussed above, eventually the strong RG flow through a nesting channel leads to a majority pairing instability. We note that this majority superfluid is not the same as proposed in previous studies of fermion gases [73, 74, 75], but is instead a lattice effect and has a much larger energy scale and critical temperature. As the density of minority species is further decreased, it starts to behave like a fermion gas, with a small, almost circular FS, as shown for example in Fig. 4.3(c). When the density of minority species becomes less than quarter filling, the induced majority BCS vertices are no longer coupled to its own nesting vertices, which causes a sudden drop of the critical temperature for the majority pairing channel. Since the majority species is still perfectly nested, there is more phase space for the minority pairing interactions to be mediated and renormalized. This crossover of RG flows is shown in Fig. 4.3(a). The majority pairing instability only exists in a small region of the phase diagram for each different majority filling, as shown in Fig. 4.1. For large minority chemical potentials, the critical temperature is much smaller, and eventually reaches our numerical limit ($\Lambda_\ell \sim 10^{-5}t$). Before this limit is reached, the flow of minority pairing is stronger than majority pairing and other channels.

4.4 Summary

We have performed a weak-coupling FRG study of a population imbalanced fermion system on a square optical lattice in two dimensions. At the weak imbalance region, the competition between spin fluctuations and intra-species attractions leads to a stripe density wave phase, rather than the usual uniform SDW phase. As the imbalance is further increased, p-wave superfluid phases become dominant due to the mismatch of the FS. Although the p-wave pairing superfluid may be expected in dilute density limit, the competition between majority and minority pairing is determined by their FS topology and the mediated intra-species pairing interaction which is renormalized from the initial bare interspecies on-site repulsive interaction. Both the stripe density wave phase and triplet superfluid phases are enhanced by nesting of the majority FS, leading to much higher critical temperatures than that found for the imbalanced Fermi gas without lattice [73, 74] at weak coupling limit. According to our calculation, the critical temperature for stripe density wave is roughly $\Lambda_c^{CDW}(\mu_\uparrow = 0, \mu_\downarrow = 0.01t) \approx 0.18t$ and that for p-wave superfluid is $\Lambda_c^{BCS_\downarrow}(\mu_\uparrow = 0.0003t, \mu_\downarrow = 0.03t) \approx 0.016t$, where the hopping amplitude t can be controlled experimentally. In a recent experiment [61], it is reported that temperatures around 6% of the Fermi temperature of a noninteracting trapped gas have been achieved. The symmetry of the order parameter of each instability can be probed by momentum-resolved spectroscopy [84, 85]. These techniques provide analogies of angle-resolved photoemission spectroscopy (ARPES) used in condensed matter systems, and can probe anisotropic systems, such as the stripe CDW and the p-wave pairing that we predict here.

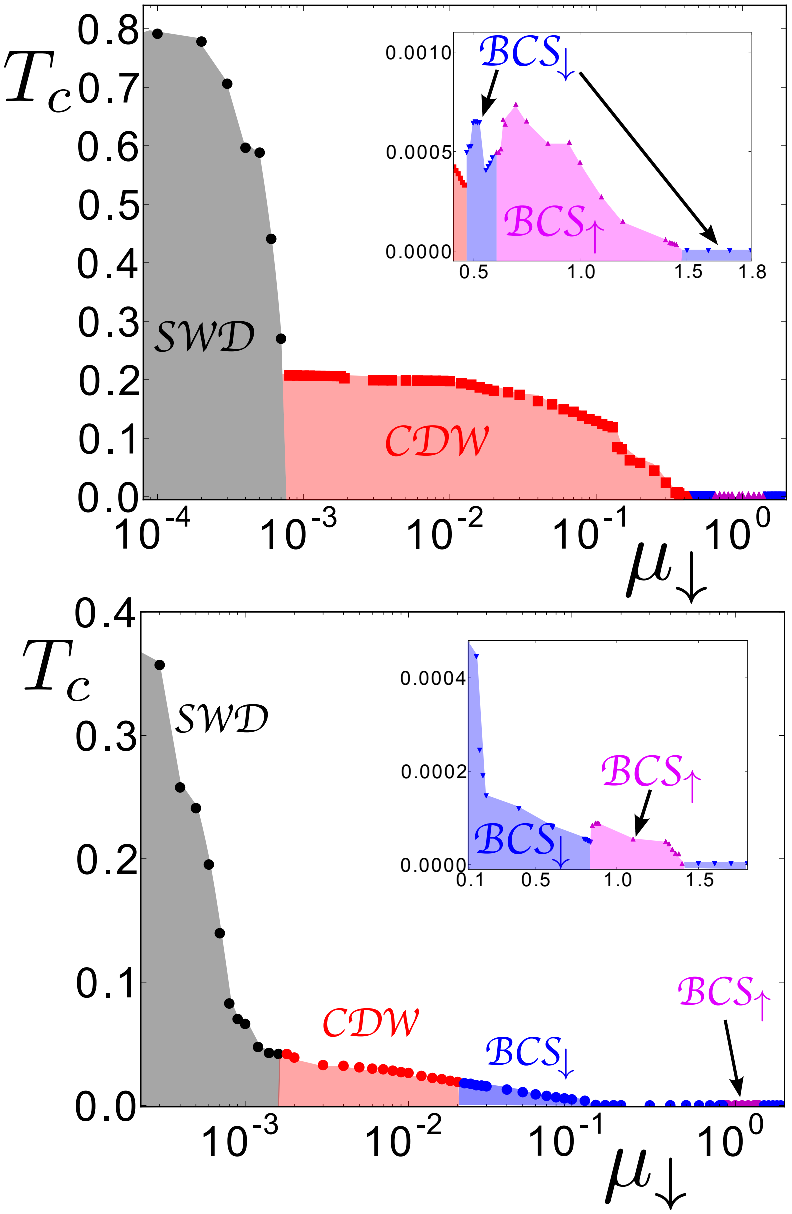

Figure 4.1: Phase diagram of spin-imbalanced fermion mixture with majority species exactly at half filling $\mu_\uparrow = 0$ (upper panel) and slightly away from half-filling $\mu_\uparrow = 0.0003t$ (lower panel). The system goes from SDW (black) at near balance to a stripe-CDW (red) as the imbalance increases. The insert shows the strong imbalance region, where single species p-wave majority (magenta) or minority (blue) pairing is the dominant instability.

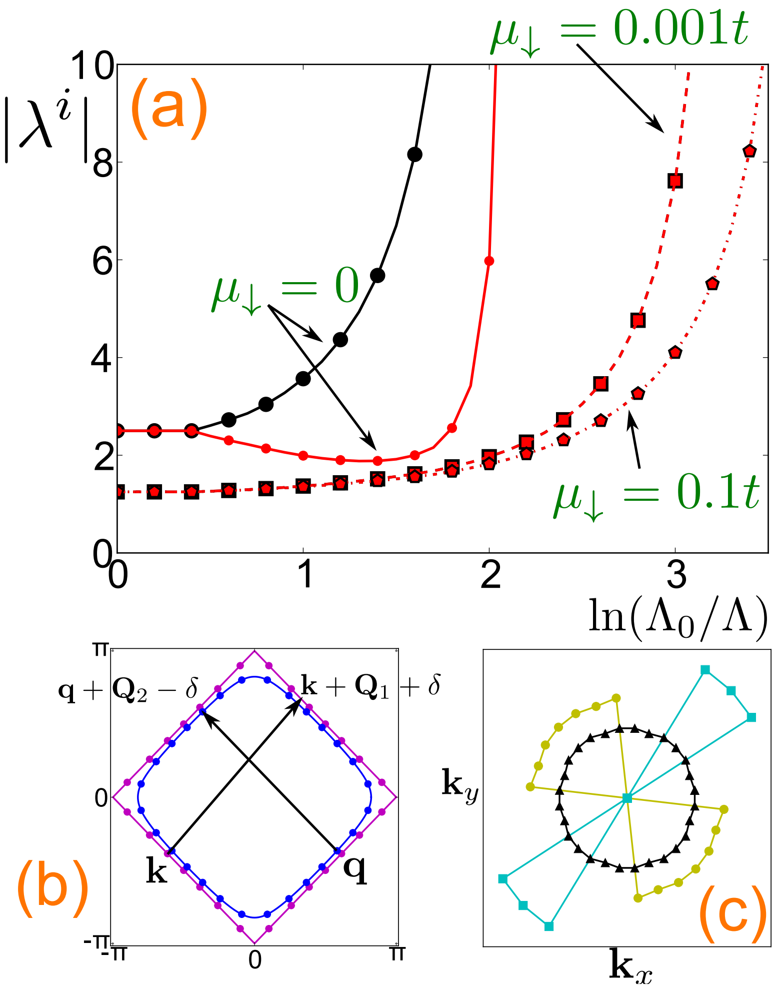

Figure 4.2: (a) RG flow of SDW$_z$ (black) and CDW (red) channels at different minority fillings, where $\mu_\downarrow = 0$ (solid line), $\mu_\downarrow = 0.001t$ (dashed line), and $\mu_\downarrow = 0.1t$ (dotted line) with majority species half-filled ($\mu_\uparrow = 0$). (b) One example of non-perfect nesting particle-hole process with net momentum $(2\pi, 0)$. (c) The symmetry of the order parameter of majority CDW (yellow circle) and minority CDW (cyan square) for the stripe-CDW phase ($\mu = 0.01t$). A conventional s-wave form factor (black triangular line) is also shown. Both species behave like stripe density wave along the diagonal direction. The circles on the FS are FRG patches.

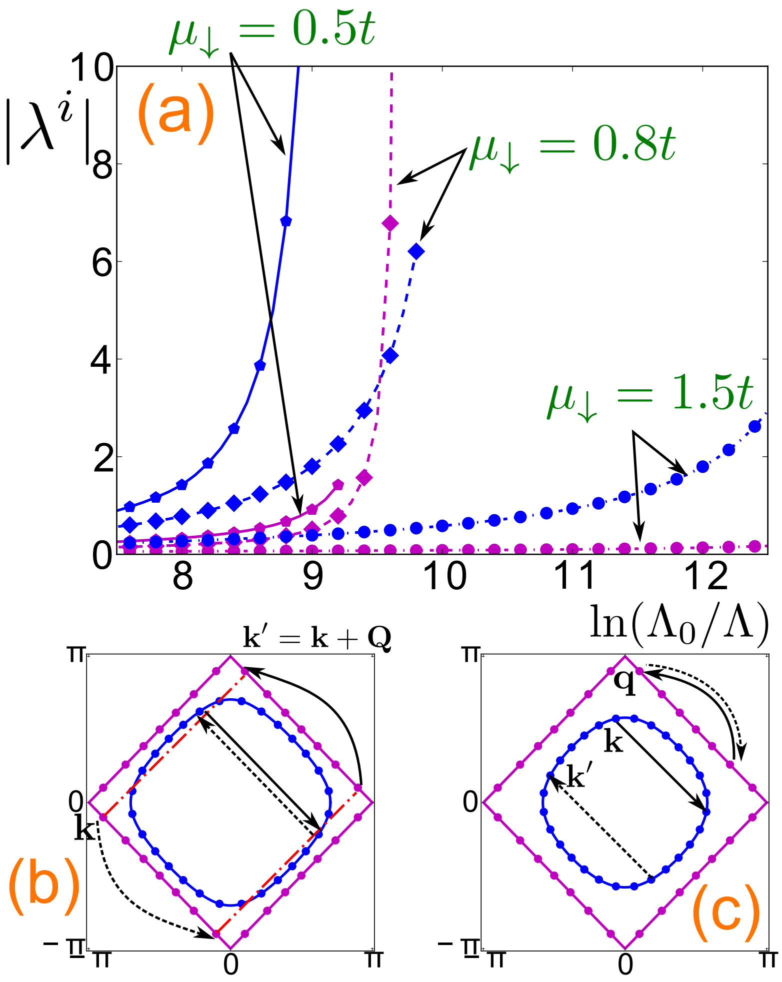

Figure 4.3: (a) RG flow of majority (magenta) and minority (blue) p-wave BCS channels at three different minority fillings, where $\mu_\downarrow = 0.5t$ (solid line), $\mu_\downarrow = 0.8t$ (dashed line), and $\mu_\downarrow = 1.5t$ (dotted line) with majority species half-filled ($\mu_\uparrow = 0$). In (b), $\mu_\downarrow = 0.8t$ (blue), the renormalized majority pairing channel $U_{\uparrow\uparrow}(\boldsymbol{k}, -\boldsymbol{k}, -\boldsymbol{k}', \boldsymbol{k}')$ couples to its own nesting channel $U_{\uparrow\uparrow}(\boldsymbol{k}, -\boldsymbol{k}, -\boldsymbol{k} + \mathbf{Q}, \boldsymbol{k} + \mathbf{Q})$. In (c), $\mu_\downarrow = 1.5t$, the half-filled majority species can provide more phase space to renormalize minority pairing channel (i.e, $\boldsymbol{q}$ can be anywhere on that FS branch).

Chapter 5

Quantum Degenerate Fermi-Fermi Mixture

5.1 Introduction

Experimental realization of quantum degenerate Fermi-Fermi mixtures have opened new arena for the study of quantum many-body phenomena in cold atom systems [62, 86, 87, 13, 88]. In these multi-component systems, many different types of fermionic superfluids have been proposed and studied [89, 90]. For imbalanced-population mixtures, a number of exotic unconventional pairing states, some of which do not occur in normal condensed-matter systems, have been investigated theoretically, such as Fulde-Ferrell-Larkin-Ovchinnikov [67, 66] superfluidity in the vicinity of phase separation [72], interior gap superfluidity [69], and *p*-wave pairing [74, 9, 73]. However, once strong Fermi surface (FS) nesting is present, instead of superconducting pairing, density wave instabilities dominate [9, 57] and may exhibit higher angular momentum order. Unconventional density waves (density waves with non-zero angular momentum) [15, 91, 92] have recently been proposed theoretically for fermionic ultracold atoms. By loading fermionic dipolar atoms [93] and molecules [94, 95, 96] onto optical lattices, unconventional density-wave instabilities may arise from the long-range and anisotropic dipole-dipole [97, 98, 99, 83, 100] or quadrupolar [101] interactions. By creating a Kagome optical lattice [40], a bond order wave can be stabilized, resulting from sublattice interference effects [102], in the presence of a sufficiently large nearest-neighbor repulsive term [41, 103].

In this chapter, we study density wave instabilities of a doubly-degenerate fermion mixture, such as ^{6}Li and ^{40}K [13, 104], on a square lattice employing a functional renormalization-group (FRG) method [3, 5, 6, 51] that takes into account inter- and intra-species interactions on an equal footing. For large intra-species repulsion, the behavior is reminiscent of a single $SU(2)$ species. When both species fermions are at half-filling, and in the presence of an inter-species repulsion sufficiently larger than the intra-species repulsion, the ground state consists of two conventional s-wave number density waves, here denoted as charge-density-wave (CDW) in analogy with number density waves in electron systems. As one species is moved away from half-filling, a d_{xy}-wave CDW instability becomes dominant. To further elucidate the physics behind the d_{xy}-CDW formation, we develop a simple four-patch model with intra- and inter-species *Umklapp* couplings that provides an analytical understanding of the competition between s- and d_{xy}-CDWs. A density imbalance between the two species of fermions in the vicinity of half-filling leads to different phase spaces for the different inter-species *Umklapp* couplings. Using reasoning similar to Shankar's phase space argument for determining one-loop RG flow equations [3], we explain how the phase-space discrepancy for the inter-species *Umklapp* couplings leads to opposite RG flows for the different intra-species *Umklapp* couplings, triggering the d_{xy}-CDW instability. By varying the densities of the two species around half-filling, we also study the range of fillings for which this regime of unconventional d_{xy}-CDW can be realized.

5.2 Model and Formalism

We start with a simple Hamiltonian describing a fermion-fermion mixture on a square lattice, $H = H_t^c + H_t^f + H_{\text{int}}$, where

$$H_t^a = -t \sum_{\langle ij \rangle, \alpha} \left(a_{i\alpha}^\dagger a_{j\alpha} + \text{H.c.} \right) - \mu_a \sum_i n_{ai}, \tag{5.1}$$

$$H_{\text{int}} = \sum_i U_{\text{cc}} n_{ci\uparrow} n_{ci\downarrow} + U_{\text{ff}} n_{fi\uparrow} n_{fi\downarrow} + U_{\text{cf}} n_{ci} n_{fi}, \tag{5.2}$$

where $a = c/f$ stands for the c/f-fermions, α is the spin index, $\langle ij \rangle$ represents nearest-neighbor pairs of sites, $n_{ai} = n_{ai\uparrow} + n_{ai\downarrow} = \sum_\alpha a_{i\alpha}^\dagger a_{i\alpha}$ and μ_a is the chemical potential of the a-fermions. For simplicity, we set nearest neighbor tunneling $t_c = t_f = t$. We consider the limit of weak repulsive interactions and employ a standard FRG method [3, 5, 6, 51] to obtain the low-energy behavior for this system, expressing the quartic terms in the resulting effective Hamiltonian in momentum space in the form

$$g_{abab}(\boldsymbol{k}_1, \boldsymbol{k}_2, \boldsymbol{k}_3, \ell) \psi_{a\alpha}^\dagger(\boldsymbol{k}_3) \psi_{b\beta}^\dagger(\boldsymbol{k}_1 + \boldsymbol{k}_2 - \boldsymbol{k}_3) \psi_{b\beta}(\boldsymbol{k}_2) \psi_{a\alpha}(\boldsymbol{k}_1) \ , \tag{5.3}$$

, where $\psi_{a\alpha}^\dagger$ is the creation operator of a-fermions in momentum space, $\boldsymbol{k} = (k_x, k_y)$, spin indices $\alpha, \beta = \uparrow, \downarrow$, species indices $a, b = c, f$ and $\ell = \ln(8t/\Lambda)$, with Λ the UV energy cut-off and $8t$ the full energy bandwidth.

5.3 Results

With fixed parameters (in units of t), $\mu_f = 0$ (half-filling) and $U_{\mathrm{ff}} = U_{\mathrm{cc}} > 0$, the phase diagram parameterized by μ_c and the dimensionless ratio of intra- and inter-species interaction $U_{\mathrm{cf}}/U_{\mathrm{ff}}$ is illustrated in Fig. 5.1. For small inter-species interactions, the species at half-filling (f-fermions) has an SDW instability. With increasing $U_{\mathrm{cf}}/U_{\mathrm{ff}}$, if both species are at half-filling, an s-wave CDW emerges, where the order parameters for the two species have a π-phase difference, referred as $s_{\pm}$-CDW here. This is analogous to the $s_{\pm}$-wave pairing in iron-pnictide superconductors [33, 14], but in the particle-hole channel. By relabeling the square lattice as a bipartite lattice with A,B sub-lattices, the real-space picture of the $s_{\pm}$-CDW phase is that $f(c)$-fermions only occupy $A(B)$ sub-lattice sites to avoid the strong inter-species repulsion.

Keeping the f-fermions at half-filling, we find phase transitions from $s_{\pm}$-CDW to d_{xy}-CDW by increasing $|\mu_c|$, and from SDW to d_{xy}-CDW by enhancing $U_{\mathrm{cf}}/U_{\mathrm{ff}}$. In Fig. 5.2(left), we show the FS of the two species for $\mu_f = 0$ and $\mu_c = -0.1$ and indicate the FS patches used in our numerical RG implementation. We also show, in the same figure, the corresponding form factors of d_{xy}-CDW for $U_{\mathrm{cf}}/U_{\mathrm{ff}} = 2.5$, obtained from decomposing the CDW coupling into eigenfunctions and plotting the dominant one close to the instability. The larger magnitude of the form factor for f-fermions indicates that the d_{xy}-instability is mainly driven by the species at half-filling, with ordering of the c-fermions resulting from a proximity effect. As we increase the density imbalance, the d_{xy}-CDW phase requires larger $U_{\mathrm{cf}}/U_{\mathrm{ff}}$ to dominate over SDW. The real-space picture of d_{xy}-CDW is sketched in

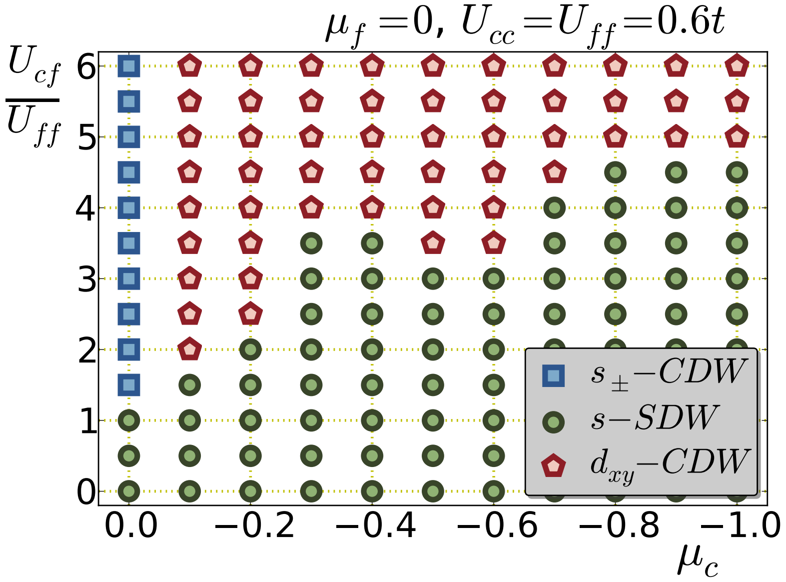

Figure 5.1: The phase diagram is parameterized by the chemical potential of c-fermions, μ_c, and the ratio of inter- and intra-species interactions, $U_{\rm cf}/U_{\rm ff}$.

Fig. 5.2(right), where the crosses indicate higher densities along next-nearest-neighbor bonds of alternating plaquettes, $O_{\rm dCDW}(\boldsymbol{r}) = e^{i\boldsymbol{Q}\cdot\boldsymbol{r}} \sum_{\alpha;i,j=\pm1} a^\dagger_\alpha(x,y) a_\alpha(x+i,y+j)$ [92].

5.3.1 4-patch toy model

To understand the physics leading to the development of the d_{xy}-CDW, we first explore the competition between the s-CDW and the d_{xy}-CDW of a single species (f-fermions) at half-filling. By decoupling the quartic interaction terms in the form $\sum_{\boldsymbol{k},\boldsymbol{p}} \mathcal{V}^{(\ell)}_{\rm CDW}(\boldsymbol{k},\boldsymbol{p}) \hat{\mathcal{O}}^\dagger_{\boldsymbol{k}} \hat{\mathcal{O}}_{\boldsymbol{p}}$, with $\hat{\mathcal{O}}_{\boldsymbol{k}}$ being a term bilinear in the fermion fields and corresponding to the order parameter of CDW, $\mathcal{V}_{\rm CDW}(\boldsymbol{k},\boldsymbol{p}) \simeq g_{\rm ffff}(\boldsymbol{k},\boldsymbol{p},\boldsymbol{p}+\boldsymbol{Q},\boldsymbol{k}+\boldsymbol{Q})$ exhibits a negative eigenvalue when CDW dominates over the SDW [33, 14]. In this case, for simplicity, we can divide the FS into four patches around $k_F = (\pi/2,\pi/2)$, $(-\pi/2,\pi/2)$ $(-\pi/2,-\pi/2)$ and $(\pi/2,-\pi/2)$ and consider

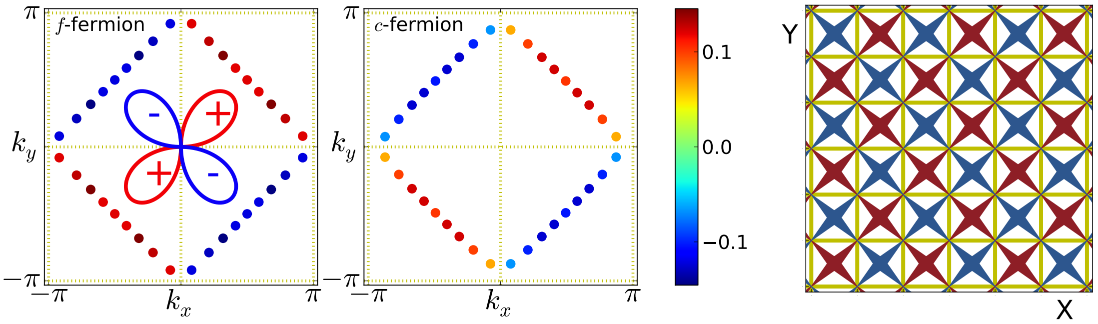

Figure 5.2: (Left) d_{xy} order parameter for f- and c-fermions. (Right) Real-space particle density of the d_{xy}-CDW state for one species of fermions.

only the scatterings occurring on these pieces of the FS (Fig. 5.3a). Under the dihedral symmetry of a square lattice, three independent *Umklapp* couplings associated with momentum transfer $\boldsymbol{k}_4 - \boldsymbol{k}_1 = \boldsymbol{Q} = (\pi, \pi)$ can be defined: $g_1 = g_{\mathrm{ffff}}(3,3,1,1)$, $g_2 = g_{\mathrm{ffff}}(1,4,2,3)$ and $g_3 = g_{\mathrm{ffff}}(1,3,3,1)$. The matrix of $\mathcal{V}_{\mathrm{CDW}}$ becomes

$$\mathcal{V}_{\mathrm{CDW}} \simeq \begin{pmatrix} g_1 & g_2 & g_3 & g_2 \\ g_2 & g_1 & g_2 & g_3 \\ g_3 & g_2 & g_1 & g_2 \\ g_2 & g_3 & g_2 & g_1 \end{pmatrix}, \tag{5.4}$$

with eigenvectors $\boldsymbol{\Phi}_s = (1,1,1,1)$, $\boldsymbol{\Phi}_d = (1,-1,1,-1)$, $\boldsymbol{\Phi}_{p_1} = (1,0,-1,0)$ and $\boldsymbol{\Phi}_{p_2} = (0,1,0,-1)$, and corresponding eigenvalues $E_s = g_1 + 2g_2 + g_3$, $E_d = g_1 - 2g_2 + g_3$ and $E_{p_{1/2}} = g_1 - g_3$. Thus, once the CDW instability is triggered, the competition between d- and s-wave channels is clear: d_{xy}-CDW (s-CDW) has the most negative eigenvalue and is therefore dominant when $g_2 > 0$ ($g_2 < 0$).

We now introduce the second species of fermions (c-fermions), with filling slightly less than half and with the FS also divided into four patches (Fig. 5.3). By introducing

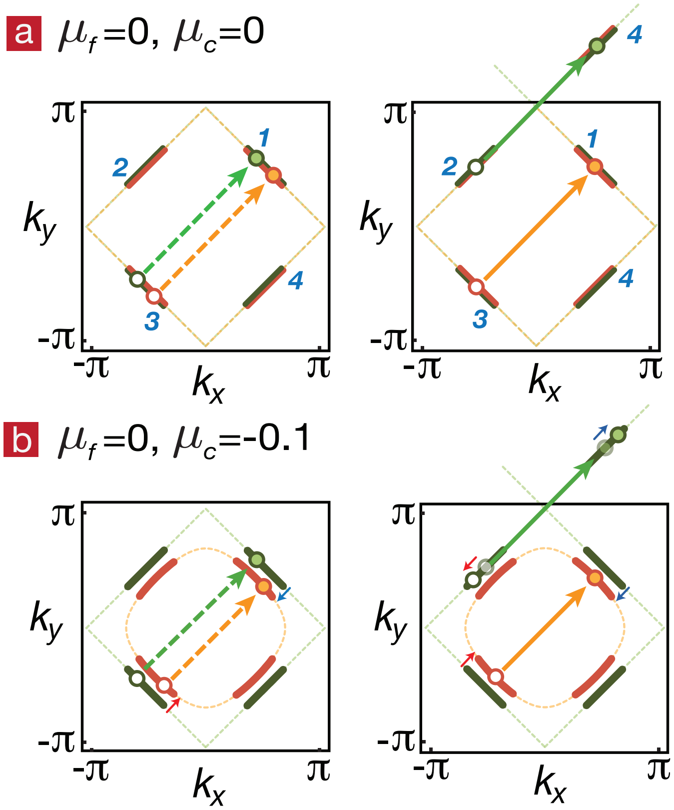

Figure 5.3: The sketches of two inter-species couplings, $g_1^{\mathrm{cf}} = g_{\mathrm{cfcf}}(3,3,1,1)$ (left) and $g_2^{\mathrm{cf}} = g_{\mathrm{cfcf}}(4,1,2,3)$ (right), for two different fillings of c-fermions. In (b), the deviation of the FS for $\mu_c = -0.1$ from the one at half-filling is intentionally enlarged for better visualization.

an inter-species interaction and defining the *Umklapp* couplings $g_1^{\mathrm{cf}} = g_{\mathrm{cfcf}}(3,3,1,1)$, $g_2^{\mathrm{cf}} = g_{\mathrm{cfcf}}(4,1,2,3)$ and $g_3^{\mathrm{cf}} = g_{\mathrm{cfcf}}(1,3,3,1)$, the one-loop RG equations for g_1 and g_2 are given by

$$\frac{dg_1}{d\ell} = \mathcal{A}_{1jk} g_j g_k + \sum_{n=1}^{3} \mathcal{B}_{1nn} \left(g_n^{\mathrm{cf}}\right)^2 + \mathcal{B}_{122} \left(g_2^{\mathrm{cf}}\right)^2, \tag{5.5}$$

$$\frac{dg_2}{d\ell} = \mathcal{A}_{2jk} g_j g_k + 2\mathcal{B}_{212} g_1^{\mathrm{cf}} g_2^{\mathrm{cf}} + 2\mathcal{B}_{223} g_2^{\mathrm{cf}} g_3^{\mathrm{cf}}, \tag{5.6}$$

where $\mathcal{A}_{ijk}$ and $\mathcal{B}_{ijk}$ are the kernels of the RG equations for intra- and inter-species couplings, respectively, and i, j, k represent coupling indices. $\mathcal{A}_{ijk}$ contains contributions from all one-loop diagrams (Figs. 2.2b to 2.2f). $\mathcal{B}_{ijk}$ corresponds to a fermionic bubble (Fig. 2.2d) for the c-fermions, obtained when two inter-species couplings are contracted to generate a correction to the intra-species f-fermion coupling. The $\mathcal{B}_{ijk}$'s are therefore always negative and correspond to an effective attractive interaction for the f-fermions, mediated by the c-fermions. Note that when the bare inter-species interaction is weak, $U_{\mathrm{cf}}/U_{\mathrm{ff}} \ll 1$, and the $\mathcal{B}_{ijk} g_j^{\mathrm{cf}} g_k^{\mathrm{cf}}$ terms can be neglected. In this case, the $\mathcal{A}_{ijk} g_j g_k$ intra-species terms eventually drive g_1 and g_2 to large positive values, leading to an SDW instability.

When both species are at half-filling, the two FS overlap and the three inter-species *Umklapp* couplings (g_1^{cf}, g_2^{cf}, g_3^{cf}) exhibit equivalent phase space; the same applies to the intra-species *Umklapp* couplings. In this circumstance, increasing the bare value of the inter-species interaction in Eq. (5.5) and (5.6) eventually leads both g_1 and g_2 to flow to negative values and gives rise the s-CDW instability. When one species is away from half-filling, the four patches on its rounded-square FS are slightly shifted from the ones at half-filling. In Fig. 5.3b, we illustrate the two FS and corresponding momentum shifts between the patches. As shown in the left panel of Fig. 5.3b, for fermions on the FS, the net momentum transfer in the inter-species process g_1^{cf} is no longer equal to a reciprocal lattice vector but has a small shortage corresponding to the shift in the position of the Fermi patches for the c-fermions. This is also true for the g_3^{cf} processes. As high-energy modes are eliminated during the RG transformation, these two couplings will have a reduced phase-space in which they can occur and are not allowed when only fermions on the FS remain. However, the shortage in the momentum transfer for scattering c-fermions across two parallel patches (momentum transfer $\boldsymbol{Q} - \boldsymbol{\delta}$) can be compensated in g_2^{cf} by having the f-fermions scatter by $\boldsymbol{Q}+\boldsymbol{\delta}$. As sketched in Fig. 5.3b (right panel), this scattering is allowed by momentum and energy conservation due to the nesting of the FS (flat parallel patches in our simple model). Thus, after moving one species away from half-filling, following Shankar's phase-space argument [3], particle-hole diagrams involving g_2^{cf} have an extended phase space in which they are non-zero, while ones involving g_1^{cf} and g_3^{cf} can be ignored to leading order in $d\Lambda$. As a consequence, the RG equations, Eq. (5.5) and (5.6), can be rewritten as $dg_1/d\ell = \mathcal{A}_{1jk} g_j g_k + 2\mathcal{B}_{122} \left(g_2^{\mathrm{cf}}\right)^2$ and $dg_2/d\ell = \mathcal{A}_{2jk} g_j g_k$, and g_2 receives no contribution from inter-species terms. The inter-species interaction term drives g_1 to a negative value (effective mediated attraction), but g_2, which is renormalized only by intra-species repulsion, still flows to positive values. The flow to negative values leads to CDW instability, and the asymmetry in the *Umklapp* components means that the CDW instability has d_{xy}-wave order parameter ($g_1 < 0$ and $g_2 > 0$).

5.3.2 Grand FRG flow

Going back to the full FRG calculation with 2×36 patches, we confirm the simple mechanism demonstrated with the four-patch model by identifying, among the RG flows for all the couplings, the ones that are most divergent and looking at their behavior. In Fig. 5.4, the RG flows of the most dominant intra-species couplings, U_{ffff}, are plotted for two different cases: c-fermions at half-filling ($\mu_c = 0$) and away from half-filling ($\mu_c = -0.1$). When both species are at half-filling, the two couplings are equal to each other and flow

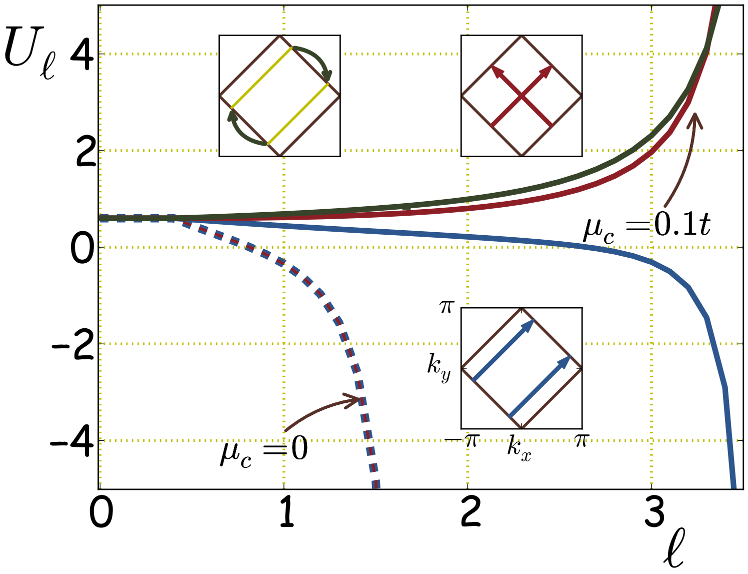

Figure 5.4: The flows of dominant nesting couplings in the RG procedure, g_{ffff}, are illustrated for $\mu_c = 0$ (dashed lines) – note that these two lines are on top of each other indicating that the two couplings have the same magnitude in this case; and $\mu_c = -0.1$ (solid lines). The three couplings are illustrated in the insets, and their flows with matched color.

to large negative values (dashed and solid blue lines), leading to the s-CDW instability. However, as expected from the four-patch analysis, once the c-fermions are away from half-filling ($\mu_c = -0.1$), the two couplings are renormalized in opposite ways (dashed and solid orange lines), resulting in d_{xy}-CDW. The population imbalance between the two fermion species in the vicinity of FS nesting provides the two FS with displaced parallel portions, which is the key ingredient for the mechanism we propose for creating a d_{xy}-CDW with purely repulsive interactions.

In our numerical calculation we obtain the RG flows of all interaction vertices with momenta lying on the Fermi surfaces. Although we can explain the d_{xy}-CDW phase using a simple four-patch model and analytical arguments involving RG flows of just a few

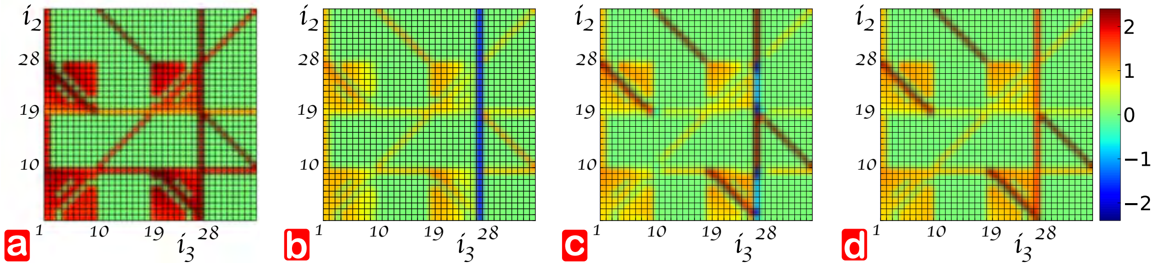

Figure 5.5: Snapshots of interaction vertices during RG flow for f-fermions at half-filling ($\mu_f = 0$). (a) $g_{\mathrm{cfcf}}(i_1 = 1, i_2, i_3)$ and (b)-(d) $g_{\mathrm{ffff}}(i_1 = 1, i_2, i_3)$. Other parameters are set to $\mu_c = 0$, $U_{\mathrm{cf}}/U_{\mathrm{ff}} = 2.0$ for (a) and (b), where the $s_{\pm}$-CDW instability occurs. In (c), $\mu_c = 0.1t$ and $U_{\mathrm{cf}}/U_{\mathrm{ff}} = 2.0$, this is in the regime where unconventional d_{xy}-wave CDW dominates. (d) $\mu_c = 0.1t$, $U_{\mathrm{cf}}/U_{\mathrm{ff}} = 0.5$, the SDW will be the instability if inter-species interaction is weak. Intra-species interactions are set to $U_{\mathrm{cc}} = U_{\mathrm{ff}} = 1.0t$ in all cases shown here.

Umklapp couplings, it is instructive to see how some of the vertex functions renormalize. In Fig. 5.5, we show a snapshot at a given "RG-time" ℓ of a few coupling functions. Since each vertex $g_{abab}(i_1, i_2, i_3, \ell)$ is a function of three free patch-indices, we fix one of them, $i_2 = 1$, where the positions of each patch on the two Fermi surfaces are illustrated in Fig.1b of the main text. For f-fermions at half-filling ($\mu_f = 0$) and fixing $U_{\mathrm{cc}} = U_{\mathrm{ff}} = t$, we show couplings for different μ_c and $U_{\mathrm{cf}}/U_{\mathrm{ff}}$ corresponding to the $s_{\pm}$-CDW, d_{xy}-CDW, and SDW phases. Fig. 5.5a and Fig. 5.5b show inter-species coupling $g_{\mathrm{cfcf}}(i_1 = 1, i_2, i_3, \ell)$ and f-fermions intra-species coupling $g_{\mathrm{ffff}}(i_1 = 1, i_2, i_3, \ell)$, respectively, for $\mu_c = 0$ and $U_{\mathrm{cf}}/U_{\mathrm{ff}} = 2.0$, corresponding to a point in the phase diagram where $s_{\pm}$-CDW occurs (see Fig. 1a in the main text). Moving the c-fermions away from half-filling leads to a region of d_{xy}-CDW. Fig. 5.5c shows the intra-species coupling $g_{\mathrm{ffff}}(i_1 = 1, i_2, i_3, \ell)$ for this case ($\mu_c = 0.1t$, $U_{\mathrm{cf}}/U_{\mathrm{ff}} = 2.0$). Decreasing the inter-species coupling from this point so that $U_{\mathrm{ff}} > U_{\mathrm{cf}}$ leads to the SDW phase. Intra-species coupling $g_{\mathrm{ffff}}(i_1, i_2, i_3, \ell)$ for this case is shown in Fig. 5.5d ($\mu_c = 0.1t$, $U_{\mathrm{cf}}/U_{\mathrm{ff}} = 0.5$).

It is easy to see from the panels in Fig. 5.5 that flows to strong coupling under RG are related to Fermi surface nesting due to commensurate filling. There are two types of such couplings. The first type contains couplings of the form $g_{\mathrm{ffff}}(1, i_2, i_2 + \mathbf{Q})$, which correspond to the four pieces of diagonal lines (dark red) in Fig. 5.5d. These couplings account for the nesting between $\boldsymbol{k}_1$ and $\boldsymbol{k}_3$, and represent the SDW channel in Eq. (2.21). The second type contains $g_{\mathrm{ffff}}(1, i_2, 27)$ couplings, which make up the vertical straight line at $i_3 = 27$ in all four panels of Fig. 5.5 (blue line in Fig. 5.5b, in particular), and are responsible for the CDW channel. One can also see some sub-dominant vertices in these figures. The pairing vertex, $g_{\mathrm{ffff}}(i_1, i_2 = -i_1, i_3)$ corresponds to the horizontal line at $i_1 = 19$. The major diagonal line at 45°, going from the lower left to the upper right corners of the panels, corresponds to the backward scattering, $g_{\mathrm{ffff}}(i_1, i_2, i_3 = i_2)$. The forward scattering, $g_{\mathrm{ffff}}(i_1, i_2, i_3 = i_1)$, is the vertical straight line located at $i_3 = 1$. Finally, there are four small squares, which are enhanced due to scattering of a particle from one patch to another belonging to the same flat side of the nested Fermi surface.

Starting from the $s_{\pm}$-CDW phase (Fig. 5.5a and 5.5b), the leading divergent couplings are of the second kind, $g_{\mathrm{ffff}}(1, i_2, 27)$, and flow to negative values (vertical line along $i_3 = 27$ in Fig. 5.5b) as we mention in the main text. The points along this vertical straight line of most divergent couplings have the same magnitude for all values of i_2, indicating an isotropic s-wave symmetry. Furthermore, the inter-species interaction, $g_{\mathrm{cfcf}}(1, i_2, 27)$, flows to strong positive values (5.5a), again with the same value for all i_1 patch indices. This sign difference between g_{ffff} and g_{cfcf} indicates that the s-wave order parameter has a π-phase between the f- and c-fermions, and thus this corresponds to an $s_{\pm}$-CDW instability.

In Fig. 5.5d, intra-species couplings are almost unaffected by weak inter-species couplings, and the strongest flow is in the SDW channel, which is represented by the four separate pieces of diagonal red lines. Finally, in Fig. 5.5c, the couplings show that the nesting process, $g_{\mathrm{ffff}}(1, i_2, 27)$, has alternating signs (red and blue in the vertical straight line at $i_3 = 27$). The sign alternation in the CDW form factor with four nodes, at $(\pm\pi, 0)$ and $(0, \pm\pi)$, corresponds to d_{xy}-wave symmetry, instead of the more usual isotropic s-wave symmetry seen in Fig. 5.5b. The physics behind the emergence of this sign change and d_{xy}-symmetry is explained in main text.

5.3.3 Critical Temperature

During the FRG calculation, the UV cutoff $\Lambda_l = \Lambda_0 e^{-l}$ is reduced as the RG scale l increases. The scale $l = l_c$ at which an instability occurs (divergent flow) provides an estimate for the critical energy (and temperature) scale for the transition[3]. We first use a small initial bare coupling, $U_{\mathrm{cc}} = U_{\mathrm{ff}} = 0.2t$, and estimate the critical temperature. The phase diagram for this case is shown in Fig. 1b of the main text. In Fig. 5.6a, we show the critical temperature from our FRG calculation as a function of the ratio $U_{\mathrm{cf}}/U_{\mathrm{ff}}$, for $U_{\mathrm{cc}} = U_{\mathrm{ff}} = 0.2t$, for a fixed value of $\mu_c = 0.2t$. This corresponds to a vertical cut of the phase diagram shown in Fig. 1b of the main text. There are two competing orders, SDW and d_{xy}-CDW, and their corresponding T_c in units of the Fermi temperature T_{F}. The critical temperatures found for this case are small, less than $10^{-2}T_{\mathrm{F}}$. However the

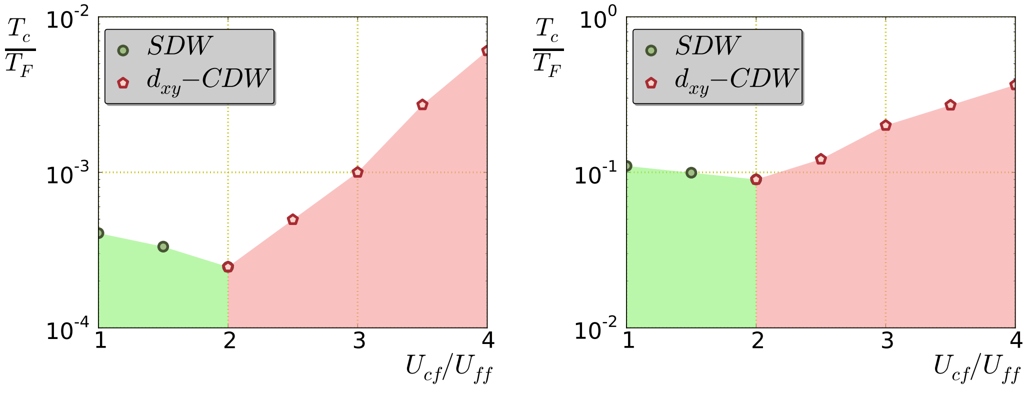

(a) $U_{\mathrm{cc}} = U_{\mathrm{ff}} = 0.2t$

(b) $U_{\mathrm{cc}} = U_{\mathrm{ff}} = t$

Figure 5.6: Critical temperatures in units of the Fermi temperature T_{F} for the dominant instabilities SDW and d_{xy}-CDW as a function of the interaction ratio $U_{\mathrm{cf}}/U_{\mathrm{ff}}$, with $\mu_f = 0$ and $\mu_c = 0.2t$.

critical temperature is significantly larger for larger bare interaction strengths, as shown in Fig. 5.6b for $U_{\mathrm{cc}} = U_{\mathrm{ff}} = t$, where T_c of the d_{xy}-CDW is more than 10% of T_{F}. Both figures (Fig. 5.6a and b) show that the T_c of SDW decreases as the ratio of initial bare interactions $U_{\mathrm{cf}}/U_{\mathrm{ff}}$ increases because it is stabilized by the on-site repulsion for the species at half-filling (f-fermions) and larger on-site inter-species repulsion U_{cf} acts against it. As the other competing order d_{xy}-CDW starts to dominate, its T_c increases as the ratio increases. Larger initial on-site inter-species repulsion U_{cf} favors the d_{xy}-CDW instability. While the FRG approach only applies to weak-couplings, that is, bare coupling strengths small compared to the full energy bandwidth of the problem (of order $8t$), the ratio of $U_{\mathrm{cf}}/U_{\mathrm{ff}}$ can be tuned to be very large, enhancing the value of T_c for d_{xy}-CDW. In a cold atom experiment, the f-fermions could be taken to be ^{6}Li or ^{40}K, for example, and the intra-species interaction $U_{\rm ff}$ can be tuned to close to zero via a Feshbach resonance with $U_{\rm cf}$ remaining positive and smaller than $8t$.

5.3.4 Robustness of the d_{xy}-CDW phase

As the calculation of T_c indicates, a sufficiently large inter-species interaction ($U_{\rm cf}$) compared to the intra-species repulsion of the species at half-filling ($U_{\rm ff}$) is needed to create the d_{xy}-CDW phase with a realistic value for T_c. However, it is not necessary to have the two intra-species interactions, $U_{\rm ff}$ and $U_{\rm cc}$, to be equal. If they are different, the phase diagram as a function of the ratio $U_{\rm cf}/U_{\rm ff}$ remains qualitatively unchanged, with no strong dependence on the value of $U_{\rm cc}$. We show the phase diagram for $U_{\rm cc} = 0$ in Fig. 5.7(a). Comparing with Fig. 1b in the main text, we see that it is qualitatively the same, with the phase boundaries only slightly shifted, and therefore the exotic d_{xy}-CDW phase is not sensitive to the c-fermion intra-species interaction.

Experimental candidates for realizing this mixture, such as ^{6}Li-^{40}K mixture, have components with different values for their physical mass. The qualitative features of the phase diagram indeed do not require $t_f = t_c$. If the c-fermion, which is the species not at half-filling, is lighter than the f-fermion, the screening effect from c-fermions becomes even more effective than in the equal mass case, and the d_{xy}-CDW phase is further enhanced. If the c-fermions are heavier, the screening effect becomes less effective and, for c-fermions much heavier than f-fermions, the d_{xy}-CDW will eventually be completely suppressed. Therefore, for a ^{6}Li-^{40}K mixture, having the ^{40}K atoms be the f-fermions (half-filled) is more favorable for the emergence of d_{xy}-CDW order. These features provide more flexibility for the experimental realization of the d_{xy}-CDW phase we predict.

The effective attractive interaction between f-fermions, mediated by the c-fermions, can also drive a BCS pairing instability if the nesting of the f-fermions FS is destroyed. To study the competition between pairing (SC) and density-wave instabilities, we explored the phase diagram parameterized by the chemical potentials of the two species, shown in Fig. 5.7(b) for $U_{\rm cc} = U_{\rm ff} = U_{\rm cf}/2.5$. The d_{xy}-CDW occurs as an intermediate phase between two limiting behaviors: $s_{\pm}$-CDW, when both species are at half-filling, and SDW, when one species is at half-filling and the other is far away from half-filling. Importantly, the d_{xy} phase persists in a reasonably wide range of fillings of the minority species.

The scale ℓ_c at which the divergence of the couplings occurs provides an estimate for the critical energy (and temperature) scale for the transition. For the d_{xy}-CDW transition we find that for $U_{\rm ff} = 0.2t$, the optimal T_c is about 0.01 T_F. For $U_{\rm ff} = t$, T_c is considerably higher, ranging from 0.1-0.4 T_F for different values of the $U_{\rm cf}/U_{\rm ff}$ ratio. Experiments with ^{6}Li-^{40}K mixtures [104] have achieved $T_{\rm Li} = 0.34T_F$ and $T_{\rm K} = 0.40T_F$. The values we find for T_c using FRG are only rough estimates, but they are of the same order of magnitude as these experimental values.

5.4 Summary

We point out that a sufficiently large inter-species interaction $U_{\rm cf}$ compared to the intra-species repulsion of the species at half-filling $U_{\rm ff}$ is needed to create the d_{xy}-CDW we propose here. However, it is not necessary to have $U_{\rm ff} = U_{\rm cc}$. If they are different, the phase

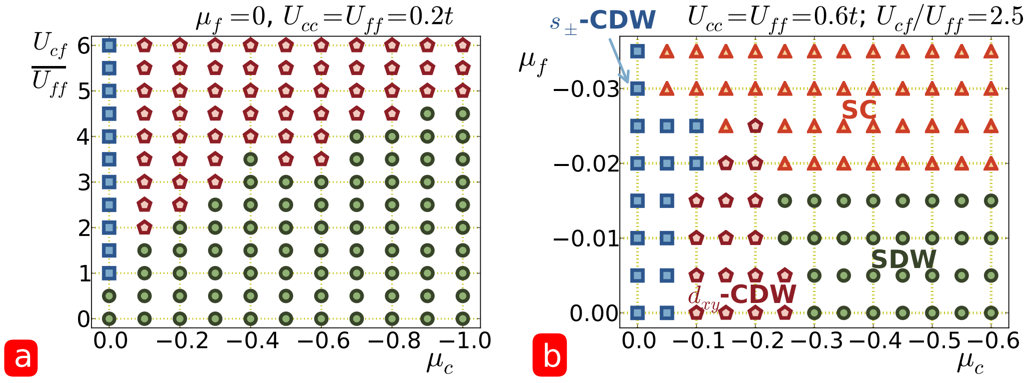

Figure 5.7: (a) The phase diagram for non-interacting c-fermions ($U_{\mathrm{cc}} = 0$), parameterized by the chemical potential μ_c, and the ratio of inter- and intra-species interactions, $U_{\mathrm{cf}}/U_{\mathrm{ff}}$. (b) The phase diagram parameterized by μ_c and μ_f. Note the large difference in scales between μ_c and μ_f.

diagram as a function of the ratio $U_{\mathrm{cf}}/U_{\mathrm{ff}}$ remains qualitatively unchanged, with no strong dependence on the value of U_{cc}. The qualitative features of the phase diagram also do not require $t_{\mathrm{f}} = t_{\mathrm{c}}$. Our predicted phase diagram should be experimentally realizable with recently achieved quantum degenerate Li-Yb [88] or Li-K mixtures [13] on a square optical lattice. Taking the ^{6}Li-^{40}K mixture, for example, with ^{40}K as the f-fermions at half-filling, one can tune U_{ff} with a magnetic Feshbach resonance ($U_{\mathrm{ff}} \simeq 0$ at around 210 Gauss). At magnetic fields in this range, the ^{6}Li - ^{6}Li interaction U_{cc} is small and repulsive, as well as the interspecies interaction U_{cf}. One can therefore use the ^{40}K Feshbach resonance to tune the $U_{\mathrm{cf}}/U_{\mathrm{ff}}$ ratio to large values, as required for our predicted d-CDW phase to occur. One may also combine magnetic field with confinement-induced resonance [105, 106, 107]. In order to avoid breaking SU(2) symmetry, optical Feshbach resonances [108, 109] may also be explored. The all optical resonance has been used in fermionic systems [110, 111], including the ^{6}Li-^{40}K mixture [13].

Identification of order parameters with nonzero angular-momentum dependence requires measurement of the relative phase between different portions of the FS. Several methods have been proposed to perform such phase-sensitive measurements [112, 84, 113, 114], including a pump-probe scheme [115] and through noise correlations[114]. The d_{xy}-CDW order parameter symmetry may also be detected via momentum-resolved spectroscopy [84, 85].

Chapter 6

Dipolar Fermions on Square Lattice of Bilayer System

6.1 Introduction

The rapid progress in trapping and cooling of ultracold magnetic atoms [93] or polar diatomic molecules [94] provides a new avenue for studying strongly correlated effects and many-body physics [116]. The magnetic dipole atoms, dysprosium, has been cooled to low temperature and reach quantum degeneracy [93]. The potassium-rubidium molecules have been achieved [94, 95], and importantly confined to 2D layers using optical lattice [117]. The advantage of loading molecules onto optical lattice is that makes system more stable from quantum chemical reaction loss due to attractive interaction [118, 117]. On the theory side, the anisotropic and long-range nature of dipole-dipole force might leads to more exotic phases or collective modes in multilayer stack at low temperature [119, 120] , including stripe density wave [121, 122], bound dimer state [123], inter-layer superfluidity [124, 125, 126], and maximally entangle state [127].

Recently, unconventional density wave has attracted great attention, especially bond-order wave [15, 102, 83]. These density waves usually are found only in a narrow parameter regime, where the frustration occurs for usual s-wave charge density wave. For example, the bond-order p-wave only exists in a small regime between charge density wave(CDW) and spin density wave in one-dimensional extended Hubbard model [24] due to strong competition between on-site and nearest neighbor repulsive interactions. Despite their ubiquity and potential importance, their physical origins and behaviors are still under debate. Several mechanism have been proposed and studied to discover unconventional density wave. Both charge- and spin bond-order-wave are found in a quantum-degenerate Fermions on kagome lattice [102, 103, 41], where the sub-lattice interference effect takes place. The other proposal is using density imbalanced Fermi-Fermi mixture [9], in which phase space discrepancy leads to d_{xy}-wave charge density wave on square lattice. Finally, fermions with dipole [83, 100] or quadruple [101, 128] nature on a 2D square optical lattice, the unconventional density wave is found for both single- and two-component system, where the long-range anisotropic nature of dipole-dipole interactions is the key ingredient. For example, half-filled single component dipole fermions on a 2D square lattice form a bond-order solid when the polar angle is tilted between two critical values [83].

In this letter, we use functional renormalization group (FRG) to study single-component dipolar fermions of bilayer with presence of square lattice. This method has been wildly used to study strongly correlated election system, such as Hubbard model [8, 6, 4], and cold atoms system under various optical lattice geometry [103, 129] and different types of interactions [83, 100, 101]. For weak couplings, density wave state relies on commensurate filling, which provides the most important feature - nested Fermi surface(FS) - to form modulations of particle wave function in real space. For dipole fermions in two dimensional bilayer geometry, the tilting angle can be controlled by applying uniform electric or magnetic fields. Also, the layer separation can be tuned by using two counter propagating lasers [116]. Under different tilting angle and layer separation, the anisotropic and long-range nature of dipole-dipole interaction within the layer and between the layers play a key role in determining quantum phases in low temperature. Interestingly, the interplay between intra- and inter-layer interactions give the exotic unconventional density wave phases. We discover the exotic bond order wave, which is out-of-phase between layers. Also, this unconventional charge density wave lives in wilder range in phase diagram than one in monolayer square lattice.

6.2 Model and Formalism

We model this single-species dipolar Fermions, with creation operator $c^\dagger$, on a quasi-two-dimensional bilayer square lattice with lattice constant a_L and layer separation l_z, saying

$$\begin{aligned}\mathcal{H} = & - t\sum_{\langle ij\rangle\alpha}(c^\dagger_{i\alpha}c_{j\alpha}+h.c.) - t_z\sum_i(c^\dagger_{i1}c_{i2}+h.c.) \\ & - \mu\sum_{i\alpha}n_{i\alpha}+\frac{1}{2}\sum_{ij\alpha\beta}V_{\alpha\beta}(\vec{r}_{ij})n_{i\alpha}n_{j\beta},\end{aligned} \tag{6.1}$$

where $\langle ij \rangle$ representing nearest neighbor sites, layer-index is $\alpha, \beta = 1, 2$, and density operator is defined as $n_{i\alpha} = c^{\dagger}_{i\alpha} c_{i\alpha}$. We assume all dipoles are aligned in the same direction $\vec{d} = d(\sin\theta_D \cos\phi_D, \sin\theta_D \sin\phi_D, \cos\theta_D)$ by applying uniform electric or magnetic field. Under this assumption, the dipole-dipole interaction $V_{\alpha\beta}(\vec{r}_{ij})$ can be determined by the two-particle *Wannier* basis, and resulted in anisotropic form

$$V_{11}(\vec{r}_{ij}) = V_{22}(\vec{r}_{ij}) = V_d \frac{1 - 3(\hat{r}_{ij} \cdot \hat{d})^2}{r_{ij}^3} \tag{6.2}$$

$$V_{12(21)} = V_d \frac{1 - 3[(\vec{r}_{ij} \pm l_z \hat{z}) \cdot \hat{d}]^2 / (r_{ij}^2 + l_z^2)}{(r_{ij}^2 + l_z^2)^{3/2}} \tag{6.3}$$

for intra- and inter-layer, where $\vec{r}_{ij} = \vec{r}_i - \vec{r}_j$ is a direction on 2D plane between two dipoles.

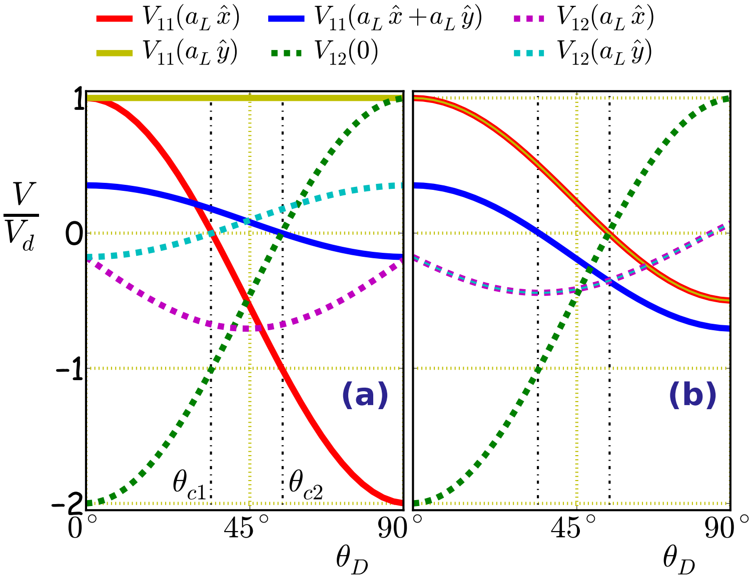

Figure 6.1: The solid (dashed) lines are magnitudes, in terms of V_d, of intra-layer V_{11} (inter-layer V_{12}) dipole-dipole interaction under different polar angle θ_D. The azimuthal angle of dipoles is set to $\phi_D = 0°$ in (a), and $\phi_D = 45°$ in (b), where layer separation is $l_z = a_L$. $V_{11}(a_L\hat{x})$ (red), $V_{11}(a_L\hat{y})$ (yellow), and $V_{12}(0)$ (green) are nearest neighbors. $V_{11}(a_L\hat{x} + a_L\hat{y})$ (blue), $V_{12}(a_L\hat{x})$ (magenta), and $V_{12}(a_L\hat{y})$ (cyan) are next-nearest neighbors. The two critical angles (black dotted lines) are $\theta_{c1} \approx 35°$ and $\theta_{c2} \approx 55°$.

In monolayer system, the low-temperature phase is mainly driven by anisotropic intra-layer interaction. From Fig. 6.1(a), we can easily see that leading intra-layer interactions (three solid lines) are all repulsive when $\theta_D < \theta_{c1}$, which results a usual checkerboard CDW. On the other end, both $V_{11}(a_L\hat{x})$ (solid red) and $V_{11}(a_L\hat{x} + a_L\hat{y})$ (solid blue) become attractive when $\theta_D > \theta_{c2}$, so the dominated low-temperature phase is triplet p_x-wave pairing. The regime between two angles is most intriguing in monolayer system, where the dominated phase is bond order solid [83]. In a bilayer system, however, the inter-layer interactions (dashed lines in Fig. 6.1) provide complicated anisotropic, even in the regime $\theta_D < \theta_{c1}$ and $\theta_D > \theta_{c2}$. As we show in the Fig. 6.1, the inter-layer interaction is attractive against the repulsive intra-layer ones, and it brings up a competition between the inter-layer pairing and in-plane conventional CDW. Similar story happens on the other end, $\theta_D > \theta_{c2}$, and question rises how inter-layer repulsion affect the intra-layer attractive interaction. Under this circumstances, the phase boundary can no long be roughly determined by just two critical angles [122].

Since we also consider the interlayer tunneling (t_z) in our model, the resulting Hamiltonian in momentum space is described by bonding and anti-bonding basis. Also, intra- and inter-band interaction will be dressed by both intra- and inter-layer interaction. For further simplicity, we mainly focus on one dipole per lattice site, saying $\mu = 0$. Thus there is (π, π) nesting between bonding and anti-bonding bands due to commensurate filling on square lattice.

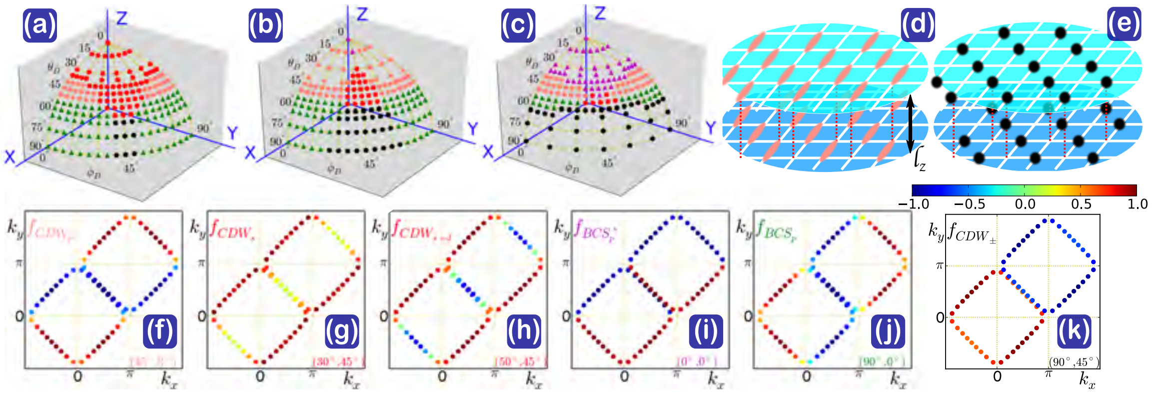

Figure 6.2: Phase diagram in terms of the dipole orientation (θ_D, ϕ_D) for half-filled single species dipolar fermions on a square lattice bilayer with layer separation (a) $l_z = 1.3a_L$, (b) $l_z = a_L$, (c) $l_z = 0.7a_L$, and the interlayer tunneling $t_z = 0.1t$. Sketched real space configuration for (d) CDW$_p$ and (e) CDW$_\pm$ with a π-phase resonance, where the dashed red lines indicate the links between upper layer and lower layer. (f)-(k) The corresponding gap symmetry forms of each instability are shown with matching color and used data points in (b) $l_z = a_L$. The magnitude (not to scale) is given by shared color bar.

6.3 Result

6.3.1 Different Inter-layer separation

We show our main result in Fig. (6.2), which contains phase diagrams obtained by FRG using $M = 36$ patches on each band. We also check the results from $M = 44$ patches, which qualitatively agree with each other. We first set layer separation $l_z = 1.3a_L$. The phase diagram is shown in Fig.6.2(a), and it is similar to the results of monolayer system [83] and phases are still separated by two critical angle roughly. For small θ_D, both layers form a conventional s-wave CDW (red circle) without sign change in gap symmetry form, which shown in f_{CDW_s} in Fig. 6.2(g). Then, the p_y-wave CDW in Fig. 6.2(f) is presence between two critical angles (pink circle in Fig. 6.2(a)). When ϕ_D is closed to 45° at the same polar angle, the conventional CDW has a mixed d-wave component, the

$f_{CDW_{s+d}}$ shown at Fig. 6.2(h). As expected, the p-wave triplet pairing (Fig. 6.2(j)) is dominated when polar angle is larger ($\theta_D > \theta_{c2}$) and azimuthal angle is not closed to 45° (green triangle in Fig. 6.2(a)). Comparing to the case in monolayer, the major difference is that we found a new phase near the regime ($\theta_D > \theta_{c2}, \phi_D \approx 45°$), where it was dominated by p-wave triplet pairing. Instead, system develops a CDW$_\pm$, black circle in Fig. 6.2(a), due to the inter-layer repulsion, which is green dashed line in Fig. 6.1(b). It is worthy to mention that the triplet pairing in monolayer system is coming from the strongest attraction along diagonal direction, which is solid blue line Fig. 6.1(b). With the presences of the second layer, however, the interlayer repulsion drives the system to conventional charge density wave, where the diagonal attraction is favor this state as well. At this point, we can see that the gap symmetry form, $f_{CDW_\pm}$ in Fig. 6.2(k), carries a π-phase resonance between two bands. That indicates two conventional CDWs in each layer, furthermore CDW at $\mathcal{A}$ sub-lattice of one layer and CDW at $\mathcal{B}$ sub-lattice of the other layer, and the real space configuration is sketched in Fig. 6.2(e).

Next, we discuss the smaller layer separation, $l_z = a_L$, and the phase diagram is shown in Fig. 6.2(b). It is easy to understand that smaller layer separation means inter-layer interaction plays a more important role, since the dipole-dipole interaction decays roughly $\sim 1/r^3$. Under this set-up, the parameter regime which was dominated by conventional CDW on the phase diagram shrinks. Instead, the dipoles which aligned perpendicular to the plane form a pairing state (magenta triangle), and it is in-phase between bands because the origin of the inter-layer attraction. Also, most part of the regime is now dominated by the unconventional p_y-wave CDW (also known as bond order solid in Ref. [83]). Interestingly, the gap symmetry form in this CDW$_p$ instability, which is shown in Fig. 6.2(f) as f_{CDW_p}, has p_y-wave form in each band and out-of-phase (π-phase resonance) between bands linked by nesting vector (π, π). In real space, we have the density modulation on alternating bonds along y-direction, which can be written as [92]

$$O_{\mathrm{CDW_p}}(\boldsymbol{r}) = e^{i\boldsymbol{Q}\cdot\boldsymbol{r}} \sum_{\alpha;i,j=\pm 1} (-1)^{\alpha} c^{\dagger}_{\alpha}(x, y) c_{\alpha}(x, y + j) \tag{6.4}$$

In Fig. 6.2(d), we show the real space configuration for this out-of-phase CDW$_p$ instability. The sing structure between bands indicates, analogy to $CDW_{\pm}$, the particle wave-function distributes on $\mathcal{A}$-$\mathcal{B}$ bond along y-direction on one layer, and $\mathcal{B}$-$\mathcal{A}$ bond on the other. Here, the physical origin that particles avoid staying on site to form a conventional s-wave CDW is frustration from other long-range interactions, since on-site density modulation is not able to minimize free energy. The reason that this exotic density wave has a larger parameter range in phase diagram is due to the bilayer effect with interlayer tunneling and long-range nature of dipole-dipole interaction. In Fig. 6.1(a), we can see the tilting polar angle changes the interaction strength. Although nearest intra-layer repulsion $V_{11}(a_L\hat{x})$ and inter-layer attraction $V_{12}(0)$ become smaller as polar angle tilts down, it favors the inter-layer next-nearest neighbor attraction $V_{12}(a_L\hat{x})$. By comparing the Figs. 6.2(a) and (b) at $\theta_D > \theta_{c2}$, we also discover that in-plane p-wave pairing is not stable against inter-layer repulsion, so $CDW_{\pm}$ dominate larger parameter regime in phase diagram than the previous case, $l_z = 1.3a_L$.

Finally, we take two layers further closed to each other to $l_z = 0.7a_L$, and show the phase diagram in Fig. 6.2(c). At this case, entire phase diagram is mostly dominated by inter-layer interaction, where small polar angle, $\theta_D < \theta_{c1}$, results in pairing due to the strong inter-layer attraction and $CDW_{\pm}$ at large polar angle, $\theta_D > \theta_{c2}$. Between two critical angles, however, both CDW$_p$ and in-plane p-wave pairing still survives. This is because this parameter regime is less affected by the inter-layer interaction , and the physics still determined by the intra-layer interaction mostly.

6.3.2 Away from Half Filling

We also study the case when dipole fermions are away from half-filling. Since there is no nesting between two FSs, which is the most important feature for density wave to develop, we can no long find any exotic density wave states. Beside that, due to the anisotropic nature of dipole-dipole interaction, attractive interaction is always presences, which would drive the system into pairing instability. If the polar angle of dipoles is smaller than critical angle θ_{c2}, the inter-layer attraction would play a key ingredient to form a p-wave pairing. On the other hand, the intra-layer would be negative if the polar angle is larger than θ_{c2}. Because the different driving process in this two triplet pairing, the resulting gap symmetry forms are different as well. In Fig. 6.2(d), we can see the deference between $f_{BCS_p^*}$ and f_{BCS_p}. The former one is in-phase under flipping orbital index, but the later one is out-phase. The inter-layer attraction trigger the p-wave pairing with symmetry form $f_{BCS_p^*}$, so the orientation of this p-wave pairing doesn't depend on the azimuthal angle ϕ_D of dipoles. The later intra-layer attraction, however, is in-plane, so the resulting pairing symmetry form will depend on the orientation of azimuthal angle ϕ_D of dipoles.

6.4 Summary

We perform the FRG calculation on single species dipolar fermions on square lattice bilayer with non-zero inter-layer tunneling. Under different tilting angles of dipoles, we discover different phases, which are related to the nature of long-range and anisotropic dipole-dipole interactions. For larger layer separation, the phase diagram is similar to the one in monolayer system, and roughly described by two critical angles. When two layers are closed to each other, the inter-layer interaction plays a important role. Due to the strong inter-layer attraction at small polar angle, the system form a paring order instead of conventional CDW. The correlated $\text{CDW}_{\pm}$ dominated when polar angle is large, because of the strong inter-layer repulsion. When the layer separation is closed to optimal regime, we discover the exotic bond order wave has a larger parameter range on phase diagram. Also this quantum state carries a π-resonance between layers. Our result shows the dipolar fermions on square lattice bilayer can realize exotic charge density wave, and observe the correlation between layers. The estimated critical temperature of these phases is around $T_c = 0.06 T_F$, which is still lower than recently experimental achievement in dysprosium [93], $T \approx 0.2 T_F$. We expect those exotic quantum phases can be observed in near future.

Probing order parameters with high angular-momentum order is always a challenge topic in condensed matter experiments. In ultracold atoms, there are several proposed methods to perform such measurements [112, 84, 113, 115, 114]. For example, a pump-probe scheme provides a phase sensitive probe of the symmetry of order parameter, which shows different pattern of the density-density correlation [115]. Moreover, analyzing two-particle interference of atom-atom density correlations, people found the related phase of different components in FS is revealed in the atomic noise correlations[114].

Chapter 7

Conclusion

In this chapter, we summarize the primary conclusions of the work we have done in the entire dissertation.

The first work in chapter 3, the phase diagram of an extended Hubbard model on a two-dimensional square lattice is shown, and low energy ground state depends on-site U, nearest-neighbor V interactions, and the filling fraction μ. From our FRG calculation, the d_{xy}-SC emerges in the regime of $U > 0$ and $V > 0$, which is in the proximity of charge-density-wave order. Upon the destruction of Fermi surface nesting, a time-reversal breaking $(p_x + ip_y)$-wave superconducting state arises when nearest-neighbor interaction is attractive $V < 0$. We show that the $(p_x + ip_y)$-SC on a square lattice under a nearest-neighbor attraction is the generic behavior when filling fraction is low which results in no Fermi surface nesting. This $(p_x + ip_y)$-SC state can be used to engineer a Majorana zero mode in the presence of a magnetic field.

The second work in chapter 4, we study the phase diagram of a spin-polarized system under different polarization (imbalance). When system is near balanced regime, the ground state remains SDW feature. As the density imbalance increases between spin-up and spin-down particles, the half-filled majority species forms a stripe density wave due to the long-range screening attractive interaction, instead of the usual SDW instability. At the strong coupling regime, the unconventional p-SC dominates over the density wave instability due to the screening long range intra-species attraction. We observed that the competition between majority and minority p-SC depends on the polarization and nesting of their Fermi surface. Also, the critical temperature of the p-SC is higher than previous studies when the imbalanced Fermi gas without presence of lattice, which believed to be Kohn-Luttinger instability.

The third work in chapter 5, we discover the unconventional d_{xy}-CDW in a quantum degenerate Fermi-Fermi mixture. When one species is half-filled and the other is slightly away, the d_{xy}-CDW dominates over conventional SDW. We proposed a four patch toy model and use phase space argument to explain the physical mechanism of formation of d_{xy}-CDW. The FRG calculation also verifies the prediction of four patch toy model and gives entire phase diagram on different interaction ratio and filling fraction of both species. We conclude that the density imbalanced between species mediates a long range attraction, which favors the half-filled species to form d_{xy}-CDW. Furthermore, we discuss the setup for this Fermi-Fermi mixture, the way to engineer large enough interaction ratio to achieve this ground state, and the potential detection can be probed if the critical temperature is reached.

The last work in chapter 6, we show phase diagrams of dipolar fermions on square lattice bilayer under different layer separations. Our results show the dipolar fermions on square lattice bilayer can realize exotic charge density wave, and observe the correlation between layers. Apparently, the inter-layer interaction changes the low energy ground state properties. We observe the competition between inter-layer pairing and charge density wave within layers when the dipoles are aligned along z-direction. When the dipoles are lying parallel to the layers, we discover the $s_{\pm}$-CDW overcome the p-wave paring due to the inter-layer repulsive interaction. Although the estimated critical temperature of these phases is still lower than recently experimental achievement in dysprosium [93]. We expect those exotic quantum phases can be observed in near future.

Finally, we establish theories that explain physical mechanism of formation of unconventional density waves and superfluities. The presence of square lattice and the density imbalanced are essential keys to these states. From several proposed models, we have show that the long range attraction in the system can favor p-SC and other higher order superfluity. This long range attraction can also affect the nearly half-filled species to form a high order charge density wave. The density imbalanced has a screening effect to other species can be the origin of the long range attraction. Despite the difficulty of engineering the long range interaction, our theory provides experiments other way to achieve the unconventional density wave and superfluity.

Bibliography

[1] I. Bloch and W. Zwerger, Rev. Mod. Phys. **80**, 885 (2008).

[2] D. Jaksch and P. Zoller, Annals of Physics **315**, 52 (2005).

[3] R. Shankar, Rev. Mod. Phys. **66**, 129 (1994).

[4] W.-M. Huang, C.-Y. Lai, C. Shi, and S.-W. Tsai, Phys. Rev. B **88**, 054504 (2013).

[5] W. Metzner, M. Salmhofer, C. Honerkamp, V. Meden, and K. Schönhammer, Rev. Mod. Phys. **84**, 299 (2012).

[6] D. Zanchi and H. J. Schulz, Phys. Rev. B **61**, 13609 (2000).

[7] C. Halboth and W. Metzner, Phys. Rev. B **61**, 7364 (2000).

[8] J. Hubbard, Electron Correlations in Narrow Energy Bands, in *Proceedings of the Royal Society A: Mathematical, Physical and Engineering Sciences*, pages 238–257, 1963.

[9] C.-Y. Lai, C. Shi, and S.-W. Tsai, Phys. Rev. B **87**, 075134 (2013).

[10] M. W. Zwierlein, A. Schirotzek, C. H. Schunck, and W. Ketterle, Science **311**, 492 (2006).

[11] G. B. Partridge et al., Phys. Rev. Lett. **97**, 190407 (2006).

[12] C.-Y. Lai, W.-M. Huang, D. K. Campbell, and S.-W. Tsai, arXiv:1307.2242 (2013).

[13] F. M. Spiegelhalder et al., Phys. Rev. A **81**, 043637 (2010).

[14] H. Zhai, F. Wang, and D. H. Lee, Phys. Rev. B **80**, 064517 (2009).

[15] D. K. Campbell, J. Gammel, and E. Loh, Phys. Rev. B **42**, 475 (1990).

[16] T. Ishiguro and K. Yamaji, *Organic superconductors*, Springer-Verlag, Berlin, 1990.

[17] H. Kiess, editor, *Conjugated Conducting Polymers*, Springer-Verlag, Berlin, 1992.

[18] J. Hirsch, Phys. Rev. Lett. **53**, 2327 (1984).

[19] M. Nakamura, Phys. Rev. B **61**, 16377 (2000).

[20] M. Tsuchiizu and A. Furusaki, Phys. Rev. Lett. **88**, 056402 (2002).

[21] P. Sengupta, A. Sandvik, and D. K. Campbell, Phys. Rev. B **65**, 155113 (2002).

[22] A. Sandvik, L. Balents, and D. K. Campbell, Phys. Rev. Lett. **92**, 236401 (2004).

[23] Y. Z. Zhang, Phys. Rev. Lett. **92**, 246404 (2004).

[24] K.-M. Tam, S.-W. Tsai, and D. K. Campbell, Phys. Rev. Lett. **96**, 036408 (2006).

[25] S. Ejima and S. Nishimoto, Phys. Rev. Lett. **99**, 216403 (2007).

[26] M. Vojta, R. Hetzel, and R. Noack, Phys. Rev. B **60**, 8417 (1999).

[27] B. Edegger, H. G. Evertz, and R. M. Noack, Phys. Rev. Lett. **96**, 146401 (2006).

[28] I. Masahiko and U. Yutaka, JPSJ **65**, 1178 (2013).

[29] P. Lemmens, G. Güntherodt, and C. Gros, Physics Reports **375**, 1 (2003).

[30] D. J. Scalapino, Rev. Mod. Phys. **84**, 1383 (2012).

[31] A. S. Alexandrov and V. V. Kabanov, Phys. Rev. Lett. **106**, 136403 (2011).

[32] D. Zanchi and H. J. Schulz, Phys. Rev. B **54**, 9509 (1996).

[33] F. Wang, H. Zhai, Y. Ran, A. Vishwanath, and D. H. Lee, Phys. Rev. Lett. **102**, 047005 (2009).

[34] S. Raghu, S. A. Kivelson, and D. J. Scalapino, Phys. Rev. B **81**, 224505 (2010).

[35] S. Raghu, E. Berg, A. V. Chubukov, and S. A. Kivelson, Phys. Rev. B **85**, 024516 (2012).

[36] R. Nandkishore, L. S. Levitov, and A. V. Chubukov, Nat Phys **8**, 158 (2012).

[37] C. Honerkamp, Phys. Rev. Lett. **100**, 146404 (2008).

[38] M. L. Kiesel, C. Platt, W. Hanke, D. A. Abanin, and R. Thomale, Phys. Rev. B **86**, 020507 (2012).

[39] M. L. Kiesel, C. Platt, W. Hanke, and R. Thomale, Phys. Rev. Lett. **111**, 097001 (2013).

[40] G.-B. Jo et al., Phys. Rev. Lett. **108**, 045305 (2012).

[41] W.-S. Wang, Z.-Z. Li, Y.-Y. Xiang, and Q.-H. Wang, Phys. Rev. B **87**, 115135 (2013).

[42] B. Uchoa and A. Castro Neto, Phys. Rev. Lett. **98**, 146801 (2007).

[43] D. A. Ivanov, Phys. Rev. Lett. **86**, 268 (2001).

[44] R. Hlubina, Phys. Rev. B **59**, 9600 (1999).

[45] J. Mráz and R. Hlubina, Phys. Rev. B **67**, 174518 (2003).

[46] S. Onari, R. Arita, K. Kuroki, and H. Aoki, Phys. Rev. B **70**, 094523 (2004).

[47] W. Kohn, Phys. Rev. Lett. **15**, 524 (1965).

[48] A. P. Kampf and A. A. Katanin, Phys. Rev. B **67**, 125104 (2003).

[49] B. Davoudi and A. M. Tremblay, Phys. Rev. B **76**, 085115 (2007).

[50] Y. Zhang and J. Callaway, Phys. Rev. B **39**, 9397 (1989).

[51] S.-W. Tsai and J. B. Marston, Can. J. Phys. **79**, 1463 (2001).

[52] C. Platt, W. Hanke, and R. Thomale, Advances in Physics **62**, 453 (2013).

[53] M. Cheng, K. Sun, V. Galitski, and S. Das Sarma, Phys. Rev. B **81**, 024504 (2010).

[54] D.-W. Wang, M. D. Lukin, and E. Demler, Phys. Rev. A **72**, 051604 (2005).

[55] L. Mathey, S.-W. Tsai, and A. Neto, Phys. Rev. Lett. **97**, 030601 (2006).

[56] K. Suzuki, T. Miyakawa, and T. Suzuki, Phys. Rev. A **77**, 043629 (2008).

[57] W.-M. Huang, K. Irwin, and S.-W. Tsai, Phys. Rev. A **87**, 031603 (2013).

[58] G. B. Partridge, W. Li, R. I. Kamar, Y. A. Liao, and R. Hulet, Science **311**, 503 (2006).

[59] M. W. Zwierlein, C. H. Schunck, A. Schirotzek, and W. Ketterle, Nature **442**, 54 (2006).

[60] Y. Shin, M. W. Zwierlein, C. H. Schunck, A. Schirotzek, and W. Ketterle, Phys. Rev. Lett. **97**, 030401 (2006).

[61] Y. A. Liao et al., Phys. Rev. Lett. **107**, 145305 (2011).

[62] Y. Shin, C. H. Schunck, A. Schirotzek, and W. Ketterle, Nature **451**, 689 (2008).

[63] W. A. Coniglio et al., Phys. Rev. B **83**, 224507 (2011).

[64] S. Uji et al., Phys. Rev. Lett. **97**, 157001 (2006).

[65] R. Casalbuoni, Rev. Mod. Phys. **76**, 263 (2004).

[66] P. Fulde and R. A. Ferrell, Phys. Rev. **135**, A550 (1964).

[67] A. I. Larkin and Y. Ovchinnikov, Sov. Phys. JETP **20**, 762 (1965).

[68] G. Sarma, J. Phys. Chem. Solid **24**, 1029 (1963).

[69] W. Liu and F. Wilczek, Phys. Rev. Lett. **90**, 047002 (2003).

[70] M. Forbes, E. Gubankova, W. Liu, and F. Wilczek, Phys. Rev. Lett. **94**, 017001 (2005).

[71] S.-T. Wu and S. Yip, Phys. Rev. A **67**, 053603 (2003).

[72] L. Radzihovsky and D. E. Sheehy, Rep. Prog. Phys. **73**, 076501 (2010).

[73] S. Raghu and S. A. Kivelson, Phys. Rev. B **83**, 094518 (2011).

[74] A. Bulgac, M. Forbes, and A. Schwenk, Phys. Rev. Lett. **97**, 020402 (2006).

[75] K. R. Patton and D. E. Sheehy, Phys. Rev. A **83**, 051607 (2011).

[76] J. K. Chin et al., Nature **443**, 961 (2006).

[77] T. Stöferle, H. Moritz, K. Günter, M. Köhl, and T. Esslinger, Phys. Rev. Lett. **96**, 030401 (2006).

[78] T. Gottwald and P. van Dongen, Phys. Rev. A **80**, 033603 (2009).

[79] B. Wunsch, L. Fritz, N. T. Zinner, E. Manousakis, and E. Demler, Phys. Rev. A **81**, 013616 (2010).

[80] M. Snoek, I. Titvinidze, and W. Hofstetter, Phys. Rev. B **83**, 054419 (2011).

[81] L. Mathey, S.-W. Tsai, and A. Castro Neto, Phys. Rev. B **75**, 174516 (2007).

[82] F. Klironomos and S.-W. Tsai, Phys. Rev. Lett. **99**, 100401 (2007).

[83] S. G. Bhongale, L. Mathey, S.-W. Tsai, C. W. Clark, and E. Zhao, Phys. Rev. Lett. **108**, 145301 (2012).

[84] T.-L. Dao, A. Georges, J. Dalibard, C. Salomon, and I. Carusotto, Phys. Rev. Lett. **98**, 240402 (2007).

[85] J. T. Stewart, J. P. Gaebler, and D. S. Jin, Nature **454**, 744 (2008).

[86] E. Wille et al., Phys. Rev. Lett. **100**, 053201 (2008).

[87] F. M. Spiegelhalder et al., Phys. Rev. Lett. **103**, 223203 (2009).

[88] H. Hara, Y. Takasu, Y. Yamaoka, J. M. Doyle, and Y. Takahashi, Phys. Rev. Lett. **106**, 205304 (2011).

[89] S. Yip, Phys. Rev. A **83**, 063607 (2011).

[90] K. Inaba and S.-i. Suga, Phys. Rev. Lett. **108**, 255301 (2012).

[91] J. B. Marston, Phys. Rev. B **39**, 11538 (1989).

[92] C. Nayak, Phys. Rev. B **62**, 4880 (2000).

[93] M. Lu, N. Q. Burdick, and B. L. Lev, Phys. Rev. Lett. **108**, 215301 (2012).

[94] K.-K. Ng et al., Science **322**, 231 (2008).

[95] A. Chotia et al., Phys. Rev. Lett. **108**, 080405 (2012).

[96] C.-H. Wu, J. W. Park, P. Ahmadi, S. Will, and M. W. Zwierlein, Phys. Rev. Lett. **109**, 085301 (2012).

[97] Y. Yamaguchi, T. Sogo, T. Ito, and T. Miyakawa, Phys. Rev. A **82**, 013643 (2010).

[98] K. Mikelsons and J. K. Freericks, Phys. Rev. A **83**, 043609 (2011).

[99] M. M. Parish and F. M. Marchetti, Phys. Rev. Lett. **108**, 145304 (2012).

[100] S. G. Bhongale, L. Mathey, S.-W. Tsai, C. W. Clark, and E. Zhao, Phys. Rev. A **87**, 043604 (2013).

[101] S. G. Bhongale, L. Mathey, E. Zhao, S. F. Yelin, and M. Lemeshko, Phys. Rev. Lett. **110**, 155301 (2013).

[102] M. L. Kiesel and R. Thomale, Phys. Rev. B **86**, 121105 (2012).

[103] M. L. Kiesel, C. Platt, and R. Thomale, Phys. Rev. Lett. **110**, 126405 (2013).

[104] M. Taglieber, A. C. Voigt, T. Aoki, T. Hänsch, and K. Dieckmann, Phys. Rev. Lett. **100**, 010401 (2008).

[105] D. S. Petrov, M. Holzmann, and G. V. Shlyapnikov, Phys. Rev. Lett. **84**, 2551 (2000).

[106] M. Olshanii, Phys. Rev. Lett. **81**, 938 (1998).

[107] H. Moritz, T. Stöferle, K. Günter, M. Köhl, and T. Esslinger, Phys. Rev. Lett. **94**, 210401 (2005).

[108] P. Fedichev, Y. Kagan, G. Shlyapnikov, and J. Walraven, Phys. Rev. Lett. **77**, 2913 (1996).

[109] J. L. Bohn and P. S. Julienne, Phys. Rev. A **56**, 1486 (1997).

[110] P. S. Julienne et al., Phys. Rev. Lett. **107**, 073202 (2011).

[111] Z. Fu et al., Phys. Rev. A **88**, 041601 (2013).

[112] I. Carusotto and Y. Castin, Phys. Rev. Lett. **94**, 223202 (2005).

[113] V. Gritsev, E. Demler, and A. Polkovnikov, Phys. Rev. A **78**, 063624 (2008).

[114] T. Kitagawa, A. Aspect, M. Greiner, and E. Demler, Phys. Rev. Lett. **106**, 115302 (2011).

[115] D. Pekker, R. Sensarma, and E. Demler, arXiv:0906.0931 (2009).

[116] M. A. Baranov, M. Dalmonte, G. Pupillo, and P. Zoller, Chem. Rev. **112**, 5012 (2012).

[117] J. L. Bohn et al., Nat Phys **7**, 502 (2011).

[118] P. S. Julienne et al., Science **327**, 853 (2010).

[119] D.-W. Wang and E. Demler, arXiv:0812.1838 (2008).

[120] Q. Li, E. H. Hwang, and S. Das Sarma, Phys. Rev. B **82**, 235126 (2010).

[121] F. M. Marchetti and M. M. Parish, Phys. Rev. B **87**, 045110 (2013).

[122] J. K. Block, N. T. Zinner, and G. M. Bruun, New J. Phys. **14**, 105006 (2012).

[123] A. G. Volosniev, N. T. Zinner, D. V. Fedorov, A. S. Jensen, and B. Wunsch, J. Phys. B: At. Mol. Opt. Phys. **44**, 125301 (2011).

[124] A. C. Potter, E. Berg, D.-W. Wang, B. I. Halperin, and E. Demler, Phys. Rev. Lett. **105**, 220406 (2010).

[125] A. Pikovski, M. Klawunn, G. V. Shlyapnikov, and L. Santos, Phys. Rev. Lett. **105**, 215302 (2010).

[126] M. A. Baranov, A. Micheli, S. Ronen, and P. Zoller, Phys. Rev. A **83**, 043602 (2011).

[127] D.-W. Wang, Phys. Rev. Lett. **98**, 060403 (2007).

[128] W.-M. Huang, M. Lahrz, and L. Mathey, Phys. Rev. A **89**, 013604 (2014).

[129] C. Honerkamp, Phys. Rev. B **68**, 104510 (2003).

Appendix A

Interaction and its symmetries

A.1 Spin-Rotation-Invariant Interaction

The most general spin-rotation-invariant interaction can be described by means of equal spin ($\sigma = \sigma'$) quantum numbers term and another with opposite spin ($\sigma = -\sigma'$) quantum number, saying $U_{\|}(\boldsymbol{k}_1, \boldsymbol{k}_2, \boldsymbol{k}_3)$ and $U_{\perp}(\boldsymbol{k}_1, \boldsymbol{k}_2, \boldsymbol{k}_3)$.

$$\sum_{\sigma} \sum_{\boldsymbol{k}_1 \boldsymbol{k}_2 \boldsymbol{k}_3} U_{\|}(\boldsymbol{k}_1, \boldsymbol{k}_2, \boldsymbol{k}_3) \bar{\Psi}_{\sigma \boldsymbol{k}_3} \bar{\Psi}_{\sigma \boldsymbol{k}_4} \Psi_{\sigma \boldsymbol{k}_2} \Psi_{\sigma \boldsymbol{k}_1} \\ + U_{\perp}(\boldsymbol{k}_1, \boldsymbol{k}_2, \boldsymbol{k}_3) \bar{\Psi}_{\sigma \boldsymbol{k}_3} \bar{\Psi}_{-\sigma \boldsymbol{k}_4} \Psi_{-\sigma \boldsymbol{k}_2} \Psi_{\sigma \boldsymbol{k}_1} \ . \tag{A.1}$$

There are other ways to write down these interaction by different quantum numbers, for example, charge-charge and spin-spin interactions,

$$\sum_{\boldsymbol{k}_1 \boldsymbol{k}_2 \boldsymbol{k}_3} U_c(\boldsymbol{k}_1, \boldsymbol{k}_2, \boldsymbol{k}_3) \bar{C}(\boldsymbol{k}_2, \boldsymbol{k}_4) C(\boldsymbol{k}_3, \boldsymbol{k}_1) + U_s(\boldsymbol{k}_1, \boldsymbol{k}_2, \boldsymbol{k}_3) \bar{\mathbf{S}}(\boldsymbol{k}_2, \boldsymbol{k}_4) \cdot \mathbf{S}(\boldsymbol{k}_3, \boldsymbol{k}_1) \tag{A.2}$$

, where basis C and component S_i are given

$$\begin{aligned} C(\boldsymbol{k}_3, \boldsymbol{k}_1) &= \sum_{\sigma} \bar{\Psi}_{\sigma \boldsymbol{k}_3} \Psi_{\sigma \boldsymbol{k}_1}, \\ S_i(\boldsymbol{k}_3, \boldsymbol{k}_1) &= \sum_{\sigma\sigma'} \bar{\Psi}_{\sigma \boldsymbol{k}_3} \sigma^i_{\sigma\sigma'} \Psi_{\sigma' \boldsymbol{k}_1} \end{aligned}$$

with *Pauli* matrixes σ^i.

Also, we can use symmetry ($|\vec{\sigma} + \vec{\sigma'}| = 0$) and anti-symmetry ($|\vec{\sigma} + \vec{\sigma'}| = \sqrt{2}$) wave functions,

$$\sum_{\boldsymbol{k}_1 \boldsymbol{k}_2 \boldsymbol{k}_3} \bar{s}(\boldsymbol{k}_4, \boldsymbol{k}_3) U_S(\boldsymbol{k}_1, \boldsymbol{k}_2, \boldsymbol{k}_3) s(\boldsymbol{k}_2, \boldsymbol{k}_1) + \sum_{\nu=0,\pm 1} \bar{t}_\nu(\boldsymbol{k}_4, \boldsymbol{k}_3) U_A(K1, \boldsymbol{k}_2, \boldsymbol{k}_3) t_\nu(\boldsymbol{k}_2, \boldsymbol{k}_1) \quad (A.3)$$

, where these states are

$$\begin{aligned} s(\boldsymbol{k}_2, \boldsymbol{k}_1) &= \frac{1}{\sqrt{2}} \sum_{\sigma} \sigma \Psi_{\sigma \boldsymbol{k}_2} \Psi_{-\sigma \boldsymbol{k}_1}, \\ t_0(\boldsymbol{k}_2, \boldsymbol{k}_1) &= \frac{1}{\sqrt{2}} \sum_{\sigma} \Psi_{\sigma \boldsymbol{k}_2} \Psi_{-\sigma \boldsymbol{k}_1}, \\ t_{\pm 1}(\boldsymbol{k}_2, \boldsymbol{k}_1) &= \Psi_{\uparrow,\downarrow \boldsymbol{k}_2} \Psi_{\uparrow,\downarrow \boldsymbol{k}_1} \ . \end{aligned}$$

Before we start to figure out their relations, we discuss the symmetry properties of interactions first. For these coupling function we just mentioned, we can define two exchange operators as

$$X\mathcal{F}(\boldsymbol{k}_1, \boldsymbol{k}_2, \boldsymbol{k}_3, \boldsymbol{k}_4) = \mathcal{F}(\boldsymbol{k}_2, \boldsymbol{k}_1, \boldsymbol{k}_3, \boldsymbol{k}_4) \quad (A.4)$$

and

$$\bar{X}\mathcal{F}(\boldsymbol{k}_1, \boldsymbol{k}_2, \boldsymbol{k}_3, \boldsymbol{k}_4) = \mathcal{F}(\boldsymbol{k}_1, \boldsymbol{k}_2, \boldsymbol{k}_4, \boldsymbol{k}_3) \quad (A.5)$$

, and time-inversion operator

$$\mathcal{T}\mathcal{F}(\boldsymbol{k}_1, \boldsymbol{k}_2, \boldsymbol{k}_3, \boldsymbol{k}_4) = \mathcal{F}(\boldsymbol{k}_3, \boldsymbol{k}_4, \boldsymbol{k}_1, \boldsymbol{k}_2) \ . \quad (A.6)$$

We can check the symmetry from Eq.(A.1). First, we check it on time-reversal

$$\mathcal{T}\sum_{\sigma\sigma'}\sum_{\boldsymbol{k}_1,\boldsymbol{k}_2,\boldsymbol{k}_3} U(\boldsymbol{k}_1\sigma,\boldsymbol{k}_2\sigma',\boldsymbol{k}_3\sigma)\bar{\Psi}_{\sigma\boldsymbol{k}_3}\bar{\Psi}_{\sigma'\boldsymbol{k}_4}\Psi_{\sigma'\boldsymbol{k}_2}\Psi_{\sigma\boldsymbol{k}_1} =$$

$$\mathcal{T}\sum_{\sigma}\sum_{\boldsymbol{k}_1\boldsymbol{k}_2\boldsymbol{k}_3}\left[U_{\|}(\boldsymbol{k}_1,\boldsymbol{k}_2,\boldsymbol{k}_3)\bar{\Psi}_{\sigma\boldsymbol{k}_3}\bar{\Psi}_{\sigma\boldsymbol{k}_4}\Psi_{\sigma\boldsymbol{k}_2}\Psi_{\sigma\boldsymbol{k}_1} + U_{\perp}(\boldsymbol{k}_1,\boldsymbol{k}_2,\boldsymbol{k}_3)\bar{\Psi}_{\sigma\boldsymbol{k}_3}\bar{\Psi}_{-\sigma\boldsymbol{k}_4}\Psi_{-\sigma\boldsymbol{k}_2}\Psi_{\sigma\boldsymbol{k}_1}\right] .$$

Then, it is easily to verify

$$L.H.S. = \sum_{\sigma\sigma'}\sum_{\boldsymbol{k}_3,\boldsymbol{k}_4,\boldsymbol{k}_1} U(\boldsymbol{k}_3\sigma,\boldsymbol{k}_4\sigma',\boldsymbol{k}_1\sigma)\bar{\Psi}_{\sigma\boldsymbol{k}_1}\bar{\Psi}_{\sigma'\boldsymbol{k}_2}\Psi_{\sigma'\boldsymbol{k}_4}\Psi_{\sigma\boldsymbol{k}_3} =$$

$$\sum_{\sigma}\sum_{\boldsymbol{k}_3\boldsymbol{k}_4\boldsymbol{k}_1}\left[U_{\|}(\boldsymbol{k}_3,\boldsymbol{k}_4,\boldsymbol{k}_1)\bar{\Psi}_{\sigma\boldsymbol{k}_1}\bar{\Psi}_{\sigma\boldsymbol{k}_2}\Psi_{\sigma\boldsymbol{k}_4}\Psi_{\sigma\boldsymbol{k}_3} + U_{\perp}(\boldsymbol{k}_3,\boldsymbol{k}_4,\boldsymbol{k}_1)\bar{\Psi}_{\sigma\boldsymbol{k}_1}\bar{\Psi}_{-\sigma\boldsymbol{k}_2}\Psi_{-\sigma\boldsymbol{k}_4}\Psi_{\sigma\boldsymbol{k}_3}\right]$$

$$= R.H.S.$$

Also, these coupling functions satisfy two symmetries, saying

$$\begin{aligned}\mathcal{T}\mathcal{F} &= \mathcal{F} \quad \text{time-inversion} &\text{(A.7)}\\ X\bar{X}\mathcal{F} &= \mathcal{F} \quad \text{exchange symmetry} &\text{(A.8)}\\ \text{also } \bar{X}\mathcal{F} &= X\mathcal{F} \quad \text{if } \mathcal{T}\mathcal{F} = \mathcal{F} . &\text{(A.9)}\end{aligned}$$

A.1.1 Parallel and antiparallel spin

In this spin-rotation-invariant interaction, we write down their basis term by term to figure out their relations. Let's start from charge and spin quantum numbers representation first. It is defined as usual for charge quantum number,

$$\begin{aligned}\bar{C}(\boldsymbol{k}_2,\boldsymbol{k}_4)C(\boldsymbol{k}_3,\boldsymbol{k}_1) &= \sum_{\sigma\sigma'}\bar{\Psi}_{\sigma'\boldsymbol{k}_4}\Psi_{\sigma'\boldsymbol{k}_2}\bar{\Psi}_{\sigma\boldsymbol{k}_3}\Psi_{\sigma\boldsymbol{k}_1} &\text{(A.10)}\\ &= \sum_{\sigma\sigma'}\bar{\Psi}_{\sigma\boldsymbol{k}_3}\bar{\Psi}_{\sigma'\boldsymbol{k}_4}\Psi_{\sigma'\boldsymbol{k}_2}\Psi_{\sigma\boldsymbol{k}_1} &\text{(A.11)}\end{aligned}$$

, and for spin quantum number,

$$\begin{aligned}\bar{\mathbf{S}}(\boldsymbol{k}_2,\boldsymbol{k}_4)\cdot\mathbf{S}(\boldsymbol{k}_3,\boldsymbol{k}_1) &= \sum_i\sum_{\sigma\sigma'}\bar{\Psi}_{\sigma\boldsymbol{k}_4}\sigma^i_{\sigma\sigma'}\Psi_{\sigma'\boldsymbol{k}_2}\sum_{\sigma''\sigma'''}\bar{\Psi}_{\sigma''\boldsymbol{k}_3}\sigma^i_{\sigma''\sigma'''}\Psi_{\sigma'''\boldsymbol{k}_1} \qquad (A.12)\\ &= \sum_i\sum_{\sigma\sigma'\sigma''\sigma'''}\sigma^i_{\sigma\sigma'}\sigma^i_{\sigma''\sigma'''}\bar{\Psi}_{\sigma''\boldsymbol{k}_3}\bar{\Psi}_{\sigma\boldsymbol{k}_4}\Psi_{\sigma'\boldsymbol{k}_2}\Psi_{\sigma'''\boldsymbol{k}_1}\ . \qquad (A.13)\end{aligned}$$

Then, we can follow above calculation by Fierz identity,

$$\sum_{i=1}^{3}(\sigma^i_{\sigma\sigma'})(\sigma^i_{\sigma''\sigma'''}) = 2\delta_{\sigma'\sigma''}\delta_{\sigma\sigma'''} - \delta_{\sigma\sigma'}\delta_{\sigma''\sigma'''} \qquad (A.14)$$

, and arrive

$$\bar{\mathbf{S}}(\boldsymbol{k}_2,\boldsymbol{k}_4)\cdot\mathbf{S}(\boldsymbol{k}_3,\boldsymbol{k}_1) = \sum_{\sigma\sigma'}(2\bar{\Psi}_{\sigma'\boldsymbol{k}_3}\bar{\Psi}_{\sigma\boldsymbol{k}_4}\Psi_{\sigma'\boldsymbol{k}_2}\Psi_{\sigma\boldsymbol{k}_1} - \bar{\Psi}_{\sigma\boldsymbol{k}_3}\bar{\Psi}_{\sigma'\boldsymbol{k}_4}\Psi_{\sigma'\boldsymbol{k}_2}\Psi_{\sigma\boldsymbol{k}_1})\ . \qquad (A.15)$$

Bring this two into Eq.(A.2), we get

$$\begin{aligned}&\sum_{\boldsymbol{k}_1,\boldsymbol{k}_2,\boldsymbol{k}_3}\sum_{\sigma}(U_c(\boldsymbol{k}_1,\boldsymbol{k}_2,\boldsymbol{k}_3) + U_s(\boldsymbol{k}_1,\boldsymbol{k}_2,\boldsymbol{k}_3)\bar{\Psi}_{\sigma\boldsymbol{k}_3}\bar{\Psi}_{\sigma\boldsymbol{k}_4}\Psi_{\sigma\boldsymbol{k}_2}\Psi_{\sigma\boldsymbol{k}_1}\\ &\qquad + \sum_{\boldsymbol{k}_1,\boldsymbol{k}_2,\boldsymbol{k}_3}\sum_{\sigma}(U_c(\boldsymbol{k}_1,\boldsymbol{k}_2,\boldsymbol{k}_3) - U_s(\boldsymbol{k}_1,\boldsymbol{k}_2,\boldsymbol{k}_3)\bar{\Psi}_{\sigma\boldsymbol{k}_3}\bar{\Psi}_{-\sigma\boldsymbol{k}_4}\Psi_{-\sigma\boldsymbol{k}_2}\Psi_{\sigma\boldsymbol{k}_1}\\ &\qquad\qquad - 2\sum_{\boldsymbol{k}_1,\boldsymbol{k}_2,\boldsymbol{k}_3}\sum_{\sigma}U_s(\boldsymbol{k}_1,\boldsymbol{k}_2,\boldsymbol{k}_3)\bar{\Psi}_{\sigma\boldsymbol{k}_3}\bar{\Psi}_{-\sigma\boldsymbol{k}_4}\Psi_{-\sigma\boldsymbol{k}_1}\Psi_{\sigma\boldsymbol{k}_2})\ . \qquad (A.16)\end{aligned}$$

The last term can be written down as

$$\sum_{\boldsymbol{k}_1,\boldsymbol{k}_2,\boldsymbol{k}_3}\sum_{\sigma}U_s(\boldsymbol{k}_2,\boldsymbol{k}_1,\boldsymbol{k}_3)\bar{\Psi}_{\sigma\boldsymbol{k}_3}\bar{\Psi}_{-\sigma\boldsymbol{k}_4}\Psi_{-\sigma\boldsymbol{k}_2}\Psi_{\sigma\boldsymbol{k}_1} \qquad (A.17)$$

, so conclusion can be made by comparing Eq.(A.1) and Eq.(A.16)

$$U_{\parallel} = U_c + U_s \qquad (A.18)$$

$$U_{\perp} = U_c - U_s - 2XU_s\ . \qquad (A.19)$$

We can solve this by setting

$$U_s = -\frac{X}{4}U_{\perp} \qquad (A.20)$$

, then we will find

$$U_c = \frac{1}{4}(2-X)U_\perp \ . \tag{A.21}$$

Next, we take this back to Eq.(A.18), and find

$$U_\parallel = \frac{1}{2}(1-X)U_\perp \ . \tag{A.22}$$

A.1.2 Singlet-Singlet and Triplet-Triplet

Second, if we use the singlet and triplet representation. From the symmetry state, which has $|\sigma + \sigma'| = 0$

$$\begin{aligned}\bar{s}(\boldsymbol{k}_4, \boldsymbol{k}_3)U_S(\boldsymbol{k}_1, \boldsymbol{k}_2, \boldsymbol{k}_3)s(\boldsymbol{k}_2, \boldsymbol{k}_1) &= \frac{1}{2}\sum_{\sigma\sigma'} U_S(\boldsymbol{k}_1, \boldsymbol{k}_2, \boldsymbol{k}_3)\bar{\Psi}_{-\sigma\boldsymbol{k}_3}\bar{\Psi}_{\sigma\boldsymbol{k}_4}\sigma\sigma'\Psi_{\sigma'\boldsymbol{k}_2}\Psi_{-\sigma'\boldsymbol{k}_1} \\ &= \frac{1}{2}\sum_{\sigma} U_S(\boldsymbol{k}_1, \boldsymbol{k}_2, \boldsymbol{k}_3)\left(\bar{\Psi}_{\sigma\boldsymbol{k}_3}\bar{\Psi}_{-\sigma\boldsymbol{k}_4}\Psi_{-\sigma\boldsymbol{k}_2}\Psi_{\sigma\boldsymbol{k}_1} - \bar{\Psi}_{\sigma\boldsymbol{k}_3}\bar{\Psi}_{-\sigma\boldsymbol{k}_4}\Psi_{\sigma\boldsymbol{k}_2}\Psi_{-\sigma\boldsymbol{k}_1}\right)\end{aligned}$$

and the anti-symmetry

$$\begin{aligned}&\sum_{\nu}\bar{t}_\nu(\boldsymbol{k}_4, \boldsymbol{k}_3)U_A(\boldsymbol{k}_1, \boldsymbol{k}_2, \boldsymbol{k}_3)t_\nu(\boldsymbol{k}_2, \boldsymbol{k}_1) = \\ &\quad U_A(\boldsymbol{k}_1, \boldsymbol{k}_2, \boldsymbol{k}_3)\left[\bar{t}_0(\boldsymbol{k}_4, \boldsymbol{k}_3)t_0(\boldsymbol{k}_2, \boldsymbol{k}_1) + \bar{t}_{+1}(\boldsymbol{k}_4, \boldsymbol{k}_3)t_{+1}(\boldsymbol{k}_2, \boldsymbol{k}_1) + \bar{t}_{-1}(\boldsymbol{k}_4, \boldsymbol{k}_3)t_{-1}(\boldsymbol{k}_2, \boldsymbol{k}_1)\right] \\ &\qquad = U_A(\boldsymbol{k}_1, \boldsymbol{k}_2, \boldsymbol{k}_3)\left[\frac{1}{2}\sum_{\sigma\sigma'}\bar{\Psi}_{-\sigma\boldsymbol{k}_3}\bar{\Psi}_{\sigma\boldsymbol{k}_4}\Psi_{\sigma'\boldsymbol{k}_2}\Psi_{-\sigma'\boldsymbol{k}_1} + \sum_{\sigma}\bar{\Psi}_{\sigma\boldsymbol{k}_3}\bar{\Psi}_{\sigma\boldsymbol{k}_4}\Psi_{\sigma\boldsymbol{k}_2}\Psi_{\sigma\boldsymbol{k}_1}\right]\end{aligned} \tag{A.23}$$

Bring them back to Eq.(A.3), we apply the relation on U_s term

$$X\sum_{\boldsymbol{k}_1\boldsymbol{k}_2\boldsymbol{k}_3}\bar{s}(\boldsymbol{k}_4, \boldsymbol{k}_3)U_S(\boldsymbol{k}_1, \boldsymbol{k}_2, \boldsymbol{k}_3)s(\boldsymbol{k}_2, \boldsymbol{k}_1) = \sum_{\boldsymbol{k}_1\boldsymbol{k}_2\boldsymbol{k}_3}\bar{s}(\boldsymbol{k}_4, \boldsymbol{k}_3)U_S(\boldsymbol{k}_1, \boldsymbol{k}_2, \boldsymbol{k}_3)s(\boldsymbol{k}_2, \boldsymbol{k}_1) \tag{A.24}$$

as well as on U_A term, and we arrive

$$\sum_{\boldsymbol{k}_1\boldsymbol{k}_2\boldsymbol{k}_3}\left[\sum_{\sigma}(U_S + U_A)\bar{\Psi}_{\sigma\boldsymbol{k}_3}\bar{\Psi}_{-\sigma\boldsymbol{k}_4}\Psi_{-\sigma\boldsymbol{k}_2}\Psi_{\sigma\boldsymbol{k}_1} + U_A\sum_{\sigma}\bar{\Psi}_{\sigma\boldsymbol{k}_3}\bar{\Psi}_{\sigma\boldsymbol{k}_4}\Psi_{\sigma\boldsymbol{k}_2}\Psi_{\sigma\boldsymbol{k}_1}\right] \quad .$$

This gives us the relation

$$\begin{aligned} U_\perp &= U_S + U_A \\ U_\parallel &= U_A \end{aligned} \tag{A.25}$$

, also the symmetry and anti-symmetry argument apply

$$\begin{aligned} U_S &= \frac{1}{2}(1+X)U_\perp \\ U_A &= \frac{1}{2}(1-X)U_\perp \ . \end{aligned} \tag{A.26}$$

A.2 Broken SU(2) Symmetry Interaction

In order to analyze the RG flow in this non-SU(2) symmetry case, we need to go back to their original basis, saying

$$C(\boldsymbol{k}_3, \boldsymbol{k}_1) = \sum_\sigma \bar{\Psi}_{\sigma \boldsymbol{k}_3} \Psi_{\sigma \boldsymbol{k}_1}, \tag{A.27}$$

$$S_i(\boldsymbol{k}_3, \boldsymbol{k}_1) = \sum_{\sigma\sigma'} \bar{\Psi}_{\sigma \boldsymbol{k}_3} \sigma^i_{\sigma\sigma'} \Psi_{\sigma' \boldsymbol{k}_1} \tag{A.28}$$

for charge and spin, and

$$s(\boldsymbol{k}_2, \boldsymbol{k}_1) = \frac{1}{\sqrt{2}} \sum_\sigma \sigma \Psi_{\sigma \boldsymbol{k}_2} \Psi_{-\sigma \boldsymbol{k}_1}, \tag{A.29}$$

$$t_0(\boldsymbol{k}_2, \boldsymbol{k}_1) = \frac{1}{\sqrt{2}} \sum_\sigma \Psi_{\sigma \boldsymbol{k}_2} \Psi_{-\sigma \boldsymbol{k}_1}, \tag{A.30}$$

$$t_{\pm 1}(\boldsymbol{k}_2, \boldsymbol{k}_1) = \Psi_{\uparrow,\downarrow \boldsymbol{k}_2} \Psi_{\uparrow,\downarrow \boldsymbol{k}_1}. \tag{A.31}$$

for singlet and triplet channel.

A.2.1 Rewrite General Interaction

The four-leg vertices can be rewritten as following,

$$\begin{aligned} V &= \sum_{1234}\sum_{\sigma\sigma'} U_{\sigma\sigma'}(1234)\bar{\psi}_{\sigma'}(3)\bar{\psi}_{\sigma}(4)\psi_{\sigma}(2)\psi_{\sigma'}(1) \\ &= \sum_{1234}\frac{1}{2}\sum_{\sigma\sigma'}\big[U_{\sigma\sigma'}(1234)\bar{\psi}_{\sigma'}(3)\bar{\psi}_{\sigma}(4)\psi_{\sigma}(2)\psi_{\sigma'}(1) \\ &\quad +U_{\sigma\sigma'}(2134)\bar{\psi}_{\sigma'}(3)\bar{\psi}_{\sigma}(4)\psi_{\sigma}(1)\psi_{\sigma'}(2)\big] \ . \qquad (A.32) \end{aligned}$$

Let us define

$$\begin{aligned} U_{\sigma\sigma'}(1234) &= U_{\sigma\sigma'} \\ U_{\sigma\sigma'}(2134) &= XU_{\sigma\sigma'} \end{aligned}$$

, and spell all terms out explicitly

$$\begin{aligned} V = \sum_{1234}\frac{1}{2}(U_{\uparrow\uparrow} - XU_{\uparrow\uparrow})\bar{\psi}_{\uparrow}(3)\bar{\psi}_{\uparrow}(4)\psi_{\uparrow}(2)\psi_{\uparrow}(1) + \frac{1}{2}(U_{\downarrow\downarrow} - XU_{\downarrow\downarrow})\bar{\psi}_{\downarrow}(3)\bar{\psi}_{\downarrow}(4)\psi_{\downarrow}(2)\psi_{\downarrow}(1) \\ + \frac{1}{2}U_{\downarrow\uparrow}\bar{\psi}_{\uparrow}(3)\bar{\psi}_{\downarrow}(4)\psi_{\downarrow}(2)\psi_{\uparrow}(1) + \frac{1}{2}U_{\uparrow\downarrow}\bar{\psi}_{\downarrow}(3)\bar{\psi}_{\uparrow}(4)\psi_{\uparrow}(2)\psi_{\downarrow}(1) \\ - \frac{1}{2}XU_{\downarrow\uparrow}\bar{\psi}_{\uparrow}(3)\bar{\psi}_{\downarrow}(4)\psi_{\uparrow}(2)\psi_{\downarrow}(1) - \frac{1}{2}XU_{\uparrow\downarrow}\bar{\psi}_{\downarrow}(3)\bar{\psi}_{\uparrow}(4)\psi_{\downarrow}(2)\psi_{\uparrow}(1) \ . \qquad (A.33) \end{aligned}$$

In order to use charge-charge and spin-spin separation, we re-write it into the following form

$$\begin{aligned} V = \sum_{1234}\frac{1}{2}(U_{\uparrow\uparrow} - XU_{\uparrow\uparrow})\bar{\psi}_{\uparrow}(3)\psi_{\uparrow}(1)\bar{\psi}_{\uparrow}(4)\psi_{\uparrow}(2) + \frac{1}{2}(U_{\downarrow\downarrow} - XU_{\downarrow\downarrow})\bar{\psi}_{\downarrow}(3)\psi_{\downarrow}(1)\bar{\psi}_{\downarrow}(4)\psi_{\downarrow}(2) \\ + \frac{1}{2}U_{\downarrow\uparrow}\bar{\psi}_{\uparrow}(3)\psi_{\uparrow}(1)\bar{\psi}_{\downarrow}(4)\psi_{\downarrow}(2) + \frac{1}{2}U_{\uparrow\downarrow}\bar{\psi}_{\downarrow}(3)\psi_{\downarrow}(1)\bar{\psi}_{\uparrow}(4)\psi_{\uparrow}(2) \\ - \frac{1}{2}XU_{\downarrow\uparrow}\bar{\psi}_{\uparrow}(3)\psi_{\downarrow}(1)\bar{\psi}_{\downarrow}(4)\psi_{\uparrow}(2) - \frac{1}{2}XU_{\uparrow\downarrow}\bar{\psi}_{\downarrow}(3)\psi_{\uparrow}(1)\bar{\psi}_{\uparrow}(4)\psi_{\downarrow}(2) \ . \qquad (A.34) \end{aligned}$$

A.2.2 Charge-Charge and Spin-Spin

By using the definition in the beginning, we can express these fields in terms of $C(\boldsymbol{k}_3, \boldsymbol{k}_1) = C(3,1)$ and $S_i(\boldsymbol{k}_3, \boldsymbol{k}_1) = S_i(3,1)$, saying

$$\begin{aligned}
\bar{\psi}_\uparrow(3)\psi_\uparrow(1) &= \frac{1}{\sqrt{2}}(C(3,1) + S_z(3,1)) && \text{(A.35)}\\
\bar{\psi}_\downarrow(3)\psi_\downarrow(1) &= \frac{1}{\sqrt{2}}(C(3,1) - S_z(3,1)) && \text{(A.36)}\\
\bar{\psi}_\uparrow(3)\psi_\downarrow(1) &= \frac{1}{\sqrt{2}}S_+(3,1) && \text{(A.37)}\\
\bar{\psi}_\downarrow(3)\psi_\uparrow(1) &= \frac{1}{\sqrt{2}}S_-(3,1)\ . && \text{(A.38)}
\end{aligned}$$

Bring these into Eq.(A.34), we have

$$\begin{aligned}
V = \sum_{1234} \frac{1}{4}\left(U_{\uparrow\uparrow} - XU_{\uparrow\uparrow} + U_{\downarrow\downarrow} - XU_{\downarrow\downarrow} + U_{\uparrow\downarrow} + U_{\downarrow\uparrow}\right)\overline{C}(2,4)C(3,1)\\
+ \frac{1}{4}\left(U_{\uparrow\uparrow} - XU_{\uparrow\uparrow} + U_{\downarrow\downarrow} - XU_{\downarrow\downarrow} - U_{\uparrow\downarrow} - U_{\downarrow\uparrow}\right)\overline{S_z}(2,4)S_z(3,1)\\
- \frac{1}{4}XU_{\uparrow\downarrow}\overline{S_+}(2,4)S_-(3,1) - \frac{1}{4}XU_{\downarrow\uparrow}\overline{S_-}(2,4)S_+(3,1)\\
+ \frac{1}{4}\left(U_{\uparrow\uparrow} - XU_{\uparrow\uparrow} - U_{\downarrow\downarrow} + XU_{\downarrow\downarrow} + U_{\uparrow\downarrow} - U_{\downarrow\uparrow}\right)\overline{S_z}(2,4)C(3,1)\\
+ \frac{1}{4}\left(U_{\uparrow\uparrow} - XU_{\uparrow\uparrow} - U_{\downarrow\downarrow} + XU_{\downarrow\downarrow} - U_{\uparrow\downarrow} + U_{\downarrow\uparrow}\right)\overline{C}(2,4)S_z(3,1) \quad \text{(A.39)}
\end{aligned}$$

, then we can conclude that

$$\begin{aligned}
V_c &= \frac{1}{4}\left(U_{\uparrow\uparrow} - XU_{\uparrow\uparrow} + U_{\downarrow\downarrow} - XU_{\downarrow\downarrow} + U_{\uparrow\downarrow} + U_{\downarrow\uparrow}\right) && \text{(A.40)}\\
V_{\sigma_z} &= \frac{1}{4}\left(U_{\uparrow\uparrow} - XU_{\uparrow\uparrow} + U_{\downarrow\downarrow} - XU_{\downarrow\downarrow} - U_{\uparrow\downarrow} - U_{\downarrow\uparrow}\right) && \text{(A.41)}\\
V_{\sigma_+} &= -\frac{1}{4}XU_{\uparrow\downarrow} && \text{(A.42)}\\
V_{\sigma_-} &= -\frac{1}{4}XU_{\downarrow\uparrow}. && \text{(A.43)}
\end{aligned}$$

A.2.3 Singlet-Singlet and Triplet-Triplet

Once again, we are going to use the definition in beginning of this chapter and use them to represent these fields, saying

$$\begin{aligned}
s(2,1) &= \frac{1}{\sqrt{2}}\left[\psi_\uparrow(2)\psi_\downarrow(1) - \psi_\downarrow(2)\psi_\uparrow(1)\right] \\
t_0(2,1) &= \frac{1}{\sqrt{2}}\left[\psi_\uparrow(2)\psi_\downarrow(1) + \psi_\downarrow(2)\psi_\uparrow(1)\right] \\
t_+(2,1) &= \psi_\uparrow(2)\psi_\uparrow(1) \\
t_-(2,1) &= \psi_\downarrow(2)\psi_\downarrow(1)
\end{aligned} \tag{A.44}$$

and

$$\begin{aligned}
\overline{s}(4,3) &= \frac{1}{\sqrt{2}}\left[\bar{\psi}_\uparrow(3)\bar{\psi}_\downarrow(4) - \bar{\psi}_\downarrow(3)\bar{\psi}_\uparrow(4)\right] \\
\overline{t}_0(4,3) &= \frac{1}{\sqrt{2}}\left[\bar{\psi}_\uparrow(3)\bar{\psi}_\downarrow(4) + \bar{\psi}_\downarrow(3)\bar{\psi}_\uparrow(4)\right] \\
\overline{t}_+(4,3) &= \bar{\psi}_\uparrow(3)\bar{\psi}_\uparrow(4) \\
\overline{t}_-(4,3) &= \bar{\psi}_\downarrow(3)\bar{\psi}_\downarrow(4)\ .
\end{aligned} \tag{A.45}$$

Therefore, the interaction will be expressed as

$$\begin{aligned}
V = \sum_{1234} & \frac{1}{2}(U_{\uparrow\uparrow} - XU_{\uparrow\uparrow})\overline{t}_+(4,3)t_+(2,1) + \frac{1}{2}(U_{\downarrow\downarrow} - XU_{\downarrow\downarrow})\overline{t}_-(4,3)t_-(2,1) \\
& \frac{1}{4}(U_{\uparrow\downarrow} + U_{\downarrow\uparrow} + XU_{\uparrow\downarrow} + XU_{\downarrow\uparrow})\overline{s}(4,3)s(2,1) \\
& \frac{1}{4}(U_{\uparrow\downarrow} - U_{\downarrow\uparrow} + XU_{\uparrow\downarrow} - XU_{\downarrow\uparrow})\overline{t}_0(4,3)t_0(2,1) \\
& \frac{1}{4}(U_{\uparrow\downarrow} - U_{\downarrow\uparrow} + XU_{\uparrow\downarrow} - XU_{\downarrow\uparrow})\overline{t}_0(4,3)s(2,1) \\
& \frac{1}{4}(U_{\uparrow\downarrow} - U_{\downarrow\uparrow} - XU_{\uparrow\downarrow} + XU_{\downarrow\uparrow})\overline{s}(4,3)t_0(2,1)\ .
\end{aligned} \tag{A.46}$$

Following by these, we can define that

$$V_{BCS}^{s} = \frac{1}{4}(U_{\uparrow\downarrow} + U_{\downarrow\uparrow} + XU_{\uparrow\downarrow} + XU_{\downarrow\uparrow}) \tag{A.47}$$

$$V_{BCS}^{t0} = \frac{1}{4}(U_{\uparrow\downarrow} - U_{\downarrow\uparrow} + XU_{\uparrow\downarrow} - XU_{\downarrow\uparrow}) \tag{A.48}$$

$$V_{BCS}^{t+} = \frac{1}{2}(U_{\uparrow\uparrow} - XU_{\uparrow\uparrow}) \tag{A.49}$$

$$V_{BCS}^{t-} = \frac{1}{2}(U_{\downarrow\downarrow} - XU_{\downarrow\downarrow}) \ . \tag{A.50}$$